Title: Dynamic structural cell responses in the thymus to acute injury, regeneration, and age

Authors: Lorenz Jahn[1]*†, Anastasia I. Kousa[1]*†, Lisa Sikkema[4,5], Angel E. Flores[6], Kimon V. Argyropoulos[1], Jennifer Tsai[2], Amina Lazrak[1], Katherine Nichols[1], Nichole Lee[1], Florent Malard[1,7], Hana Andrlova[1], Antonio L.C. Gomes[1], Enrico Velardi[1,8], Salma Youssef[1], Marina B. da Silva[1], Melissa Docampo[3], Roshan Sharma[4], Linus Mazoutis[4], Manu Setty[4,9], Dana Pe'er[4], Nancy R. Manley[6], Jarrod A. Dudakov[10,11]*‡, Marcel R.M. van den Brink[1,2,3]*‡

Affiliations:

[1]Department of Immunology, Memorial Sloan Kettering Cancer Center, New York, NY, USA.

[2]Department of Medicine, Memorial Sloan Kettering Cancer Center, New York, NY, USA.

[3]Department of Immunology and Microbial Pathogenesis, Weill Cornell Medical College; New York, NY USA and Department of Immunology, Sloan Kettering Institute; New York, NY, USA

[4]Computational and Systems Biology Program, Sloan Kettering Institute; 417 E 68th St, New York, NY, 10027.

[5]Institute of Computational Biology, Helmholtz Center Munich; Munich, Germany

[6]Department of Genetics, University of Georgia; Athens, GA, 30602, USA.

[7]INSERM U938, Centre de Recherche Saint-Antoine, Paris, Sorbonne Université, Paris, and Service d'Hématologie Clinique, AP-HP, Hôpital Saint-Antoine, Paris, France.

[8]Department of Pediatric Hematology and Oncology, Bambino Gesù Children's Hospital, IRCCS, Rome, 00146, Italy

[9]Basic Sciences Division & Translational Data Science Integrated Research Center, Fred Hutchinson Cancer Research Center, Seattle WA 98109.

[10]Program in Immunology, Clinical Research Division, Fred Hutchinson Cancer Research Center, Seattle WA 98109

[11]Department of Immunology, University of Washington, Seattle WA 98109

*Corresponding authors. Email: kousaa@mskcc.org; lorenz.jahn@gmail.com; jdudakov@fredhutch.org; VandenbM@mskcc.org

†, ‡ These authors contributed equally to this work.

SUMMARY

The thymus, the primary site of T cell development, is extremely sensitive to insult but also harbors tremendous capacity for repair. Using single cell sequencing of thymic structural cells, as well as functional and structural analyses, we revealed distinct regenerative programs by endothelial and mesenchymal subsets after injury that stimulated epithelial repair; the compartment primarily supporting T cell development. Thymic function not only declined over lifespan, contributing to immune aging, but the capacity of the thymus to regenerate after damage also declined in old mice. This could be attributed to an inability of the old microenvironment to induce reparative programs; leading to reduced ability to restore tissue structure and function. These findings provide a detailed framework for the response of structural cells to aging and acute damage, which could have considerable implications for our understanding of aging immunity and recovery from treatments such as chemotherapy and bone marrow transplant.

KEYWORDS

Thymus; atlas; structural cells; damage; aging; regeneration

INTRODUCTION

T cell development requires the close interaction between thymocytes and supporting structural (epithelial, endothelial, and mesenchymal) cells that comprise the thymic microenvironment (Kadouri et al., 2020). However, despite the importance of the thymus for generating a healthy and broad T cell repertoire, generation of new T cells declines precipitously with age as a result of age-related thymic involution, a chronic form of injury that starts in puberty and results in a significant loss of size and cellularity, disrupted stromal architecture, and ultimately reduced export of new naïve T cells and reduced responsiveness to new antigens (Douek et al., 1998; Hale et al., 2006; Rodewald, 1998). Along with its chronic decline in function with age, the thymus is also extremely sensitive to acute damage due to infection or common cancer therapies such as cytoreductive chemo- or radiation therapy. Nonetheless, the thymus has a remarkable capacity for repair after acute insults (Granadier et al., 2021; Velardi et al., 2021).

The molecular mechanisms underlying declining thymic function with age and regeneration after damage are poorly understood (Baran-Gale et al., 2020; Granadier et al., 2021; Kinsella and Dudakov, 2020; Velardi et al., 2021). Recent advances in single cell technology have allowed in-depth exploration of the heterogeneity encompassing the thymic epithelium in young (Bornstein et al., 2018; Brennecke et al., 2015; Dhalla et al., 2020; Miragaia et al., 2018) and aged subsets (Abramson and Anderson, 2017), which orchestrates the generation of T cells and their dysfunction is directly linked to autoimmunity and immunodeficiency. However, while recent studies have started to characterize the contribution of the endothelial and mesenchymal compartments to thymic development, aging and regeneration (Buono et al., 2016, 2018; Nitta and Takayanagi, 2021; Wertheimer et al., 2018), their importance in regulating these biological

processes is still largely unexplored. Finally, to the best of our knowledge no studies have investigated whether the endogenous regenerative capacity of the thymus after damage is also affected by aging.

Here we used single cell RNA sequencing (scRNA-seq) of 75,595 cells in conjunction with downstream functional and structural analysis to interrogate responses of thymic structural cell compartments (Krausgruber et al., 2020) (comprising epithelial, endothelial and mesenchymal cells) at baseline, over lifespan, and after acute injury. Using these approaches we found heretofore unknown heterogeneity -especially within the endothelial and fibroblast compartments- and identified their declining production of thymopoietic factors with age, as well as the attenuation of regenerative responses after injury.

RESULTS

Distinct baseline subsets of endothelial, epithelial and mesenchymal compartments

Although recent work has captured some of the heterogeneity of the thymic epithelial subsets (Bornstein et al., 2018; Brennecke et al., 2015; Dhalla et al., 2020; Miragaia et al., 2018), including with age (Abramson and Anderson, 2017), to characterize the entire structural cell compartment, 10,340 cells of non-hematopoietic origin (CD45^{+} depleted thymic stroma, Figure 2A and Methods) from 2-month-old (2-mo) mice were analyzed by single-cell sequencing. Primary structural cell lineages were identified based on canonical markers: thymic epithelial cells (TECs); [*Epcam*, *H2-Aa*]; endothelial cells (ECs); [*Pecam1*, *Cdh5*]; fibroblasts (FBs); [*Pdgfra*] (Figure 1B and C); and less abundant stromal subsets, including mesothelial cells (MECs); [*Upk3b*, *Nkain4*]; vascular smooth muscle cells (vSMCs); [*Acta2*, *Myl9*]; rare non-myelinating Schwann cells (nmSCs); [*Gfap*, *Ngfr* (p75) , *S100b*] (Hu et al., 2018) ; and pericytes (PCs); [*Myl9*, *Acta2*] (Zachariah and Cyster, 2010) (Figure 1B and C). To explore the underlying heterogeneity of the major CD45- stromal cell types (TECs, ECs and FBs), we first subsetted and reanalyzed each population separately. However, since certain subsets didn't have adequate cell numbers with aging or after damage, we grouped subsets with similar profiles to allow meaningful comparisons.

The epithelium comprised 11 TEC clusters (TEC1-11, Figure 1D), which closely resembled recent findings (Baran-Gale et al., 2020; Bornstein et al., 2018; Brennecke et al., 2015; Dhalla et al., 2020; Miragaia et al., 2018; Sansom et al., 2014), as illustrated by subset-specific gene signatures from these studies mapped on our data (Figure S1A to C, data S1). Our mapped clusters were next annotated based on the combined nomenclature from these studies; TEC1 as

cortical TEC (cTEC), TEC3-4 as pre-*Aire* mTEC (mTEC1), TEC5 as proliferating mTEC (mTEC-prol), TEC6-7 as Aire^{high} mTEC (mTEC2), TEC8 as *Spink5*$^{+}$ mTEC (mTEC3), TEC10 as neural TEC (nTEC) and TEC11 as tuft-like (mTEC4) (Figure 1D). Notably, TEC9 (mapping to the GP2-preferred cluster in Figure S1B) was enriched for a gene signature of microfold (M) cells of the small intestine (Haber et al., 2017) (M-like TEC, Figure 1D), adding to the enterocrine-like or neural (nTEC) (Baran-Gale et al., 2020) and tuft-like (mTEC4) (Bornstein et al., 2018) TEC subsets that share molecular profiles with epithelial cells of the small intestine (Figure S1D, data S1). TEC2 was revealed as a rare subset (TECx, Figure 1D), that uniquely expressed genes linked to extracellular matrix (ECM) (*Dcn*, *Mgp*, *Ctsl*, *Bcam*) and lipid-binding (*Apoe*, *Gas6*, *Pltp*) (data S2), which was also reflected by pathway analysis that showed enrichment for ECM and insulin-related pathways (Figure S1E). Consistent with previous work, pseudo-temporal ordering of our mTEC subsets -after removal of the small cTEC population and the more distinct TEC2 and TEC9-11 islands- reflected the distinct but progressive maturation states of mTECs (Dhalla et al., 2020) (Figure 1E, data S2).

Unsupervised clustering analysis separated endothelial cells (EC) into 10 subsets that were annotated on gene signatures from an organ-wide murine EC atlas (Kalucka et al., 2020) (Figure S1G, data S1) as arterial (arEC, EC1-EC3), capillary (capECs, EC4-EC8) and venous EC (venEC, EC9-EC10) (Figure 1F). CapEC clusters EC6-EC8 highly expressed *Plvap*, characteristic of fenestrated (f) capECs (Gordon et al., 2019) (capEC-f, Figure 1F), while clusters EC4 and EC5 expressed the continuous capEC markers (*Cldn5*, *Gja4*) and were annotated as continuous (capEC-c, Figure 1F). Less than 1% of all ECs showed enrichment for lymphatic markers (Figure S1G), in compliance with rare detection of lymphatic thymic ECs in cross

sections or by flow cytometry in adult mice (Zachariah and Cyster, 2010). Both capEC-f and capEC-c subsets were enriched for genes involved in fatty acid and glycerol uptake/metabolism (Figure S1F) -similar to capECs in the colon and small intestine (Kalucka et al., 2020)-, while capEC-f subcluster EC8 showed a unique expression pattern for *Esm1*, *Plpp1/3*, *Nrp1* and *Cd24a* (Figure S1F), distinct markers expressed in the choroid plexus ECs of the brain (Bosma et al., 2018; Bowyer et al., 2013; Kalucka et al., 2020). VenECs and arEC subcluster EC1 demonstrated the highest expression of *Vwf* and *Vcam1* (Figure 1F), genes that correlate with the vessel diameter, and thus were further identified as the largest vessels across all EC subsets. venECs also expressed high levels of P-selectin (*Selp*) and low levels of *Ly6c1* (Figure 1F), indicative of thymic portal ECs (TPECs) (Shi et al., 2016), which have been linked to homing of hematopoietic progenitors in the thymus (Chen et al., 2004; Penit and Ezine, 1989; Zlotoff et al., 2011). Notably, BMP4, which is produced by thymic ECs and is involved in regeneration after acute insult (Wertheimer et al., 2018), was expressed highest by venECs with low expression by a subset of arECs (EC1) (Figure 1F). Similar to other tissues (Kalucka et al., 2020; Vanlandewijck et al., 2018), pseudo-temporal ordering of EC subsets reflected their putative size and anatomical topology alongside the arteriovenous zonation, with arECs connecting to capECs-c/f and sequentially to venECs (Figure 1G). Capillary gene signatures were less distinctive of the thymic capillary subsets, in alignment with the existence of fewer conserved markers in capillaries of different organs (Kalucka et al., 2020).

Within the *Pdgfra*-expressing mesenchyme, we identified 11 fibroblast clusters (Figure 1H). Clusters FB1-3 displayed enrichment for gene signatures consistent with mouse capsular or human interlobular FBs (Figure S1H, data S1) (Nitta et al., 2020; Park et al., 2020), including

markers such as *Dpp4*, *Smpd3* and *Pi16* (Figure 1H). Clusters FB10 and FB11 were enriched for gene signatures indicative of mouse medullary or human perilobular FBs (Figure S1H, data S1) (Nitta et al., 2020; Park et al., 2020), including the marker genes *Ptn* and *Postn* (Figure 1H); these medullary FB subsets have been recently implicated as a source of self-antigens during negative selection (Nitta et al., 2020). A lower gradient of the mouse capsular (human interlobular) FBs gene signatures was apparent across clusters FB5-8, as well as high expression of *Gpx3*, *Ar*, *Atf3* and *Mfap4* genes, whereas clusters FB4 and FB9 demonstrated the highest enrichment for the human perilobular FB signature and highly expressed *Inmt*, *Sfrp1* and *Mfap4* (Figure 1H, Figure S1H, data S1). Pseudo-temporal ordering of the FB subsets starting from the capsFBs (Figure1I) was consistent with their putative anatomical location within the thymus as either in the sub-capsule or medulla (Nitta et al., 2020). To facilitate downstream analysis, we combined clusters FB1-3 as a single capsular FB subset (capsFB), and clusters FB10-11 as a medullary subset (medFB), while we annotated FB5-8 as cortical CMJ FBs (cor-cmjFBs) and FB4 and FB9 to as medullary CMJ FBs (med-cmjFB) based on their pseudotime proximity to the capsular or medullary subsets.

Immunohistochemistry confirmed that venECs ($CD31^+$ P-sel^+) lined large vessels located at the corticomedullary junction (CMJ) of the thymus (Figure 1J), which is consistent with their role in hematopoietic progenitor entry (Shi et al., 2016). Highest expression of PTN marked the inner medulla of the thymus, in agreement with *Ptn* expression within the FB subsets and their pseudo-temporal ordering. MFAP4 marked fibroblastic cells located in the cortex, medulla and the CMJ (Figure 1K). Functional enrichment of the top differentially expressed genes (DEGs) predicted functional heterogeneity among the FB subsets (Figure 1L). CapsFBs expressed genes associated with organ development and structure, cor-cmjFBs with insulin-like growth factor signalling,

medFBs with pathways regulating immune processes, and med-cmjFBs with vascularization and fibroblast proliferation. In conclusion, this analysis outlines the heterogeneity of structural cells in the thymus at steady state and provides insights regarding their localization and function.

Emergence of novel epithelial and partial EMT populations with hallmarks of aging

Thymic involution is a well-studied phenomenon that results in chronic decline in thymic function over lifespan (Boehm and Swann, 2013; Granadier et al., 2021; Nikolich-Zugich, 2008; Velardi et al., 2021). Total thymic cells declined in female mice across their lifespan (2, 3, 6, 8, 9, 13, 19, 22 and 24 months) (Figure 2A), with related morphological changes in the organ architecture such as a relative decrease of cortical-to-medullary area and reduction in cellular density in the cortical region (Ventevogel and Sempowski, 2013) (Figure 2B and C). Cellularity dynamics of the major structural cell lineages (TEC, EC and FB) revealed a clear pattern of reduction in the TEC compartment that mirrors the overall loss of thymic cellularity, with a more severe loss in mTECs compared to cTECs leading to a compositional change (Figure 2D). The endothelium and fibroblast compartments did not show any significant alterations. We then selected two representative ages (2-mo; young, 18-mo; old) to perform further analysis within these compartments. Flow cytometric analysis informed by the structural cell heterogeneity observed in the scRNA-seq data from 2-mo mice at steady-state (Figure 1B, D, F and H) revealed age-dependent changes in the 18-mo mice; we found a loss of the mTEC1-4 subsets (Figure 2E), consistent with recent work showing a block in mTEC lineage differentiation with aging (Baran-Gale et al., 2020). However, we observed the emergence of a novel population of EPCAM^{+} cells that lacked expression of MHCII that we refer to as age-associated TECs (aaTECs) (Figure 2E, Figure S2F), that consistently expanded within the EPCAM+ TEC

compartment when observed across lifespan (Figure 2F). Despite the profound loss of cellularity in the thymus with age, there was surprisingly little difference in cell composition within the EC compartment (Figure 2G), while medFBs, vSMCs and PCs increased in frequency and number with aging (Figure 2H and I).

Next, we profiled 11,019 CD45- thymic stroma cells from 18-mo mice by scRNA-seq and combined these with the analysis of thymi from 2-mo mice (Figure 3A and B). All cell types and subsets observed in the thymic stroma of young mice were represented within the aged cohort as instructed by canonical markers and the 2-mo cell subset gene signatures overlay on the 18-mo thymic stroma (Figure S3A to H). Consistent with our flow cytometry data (Figure 2E), we observed the emergence of distinct populations of TECs in sequencing data from the 18-mo mice, named aaTEC1-4 (Figure 3B). These novel aaTEC subsets were uniquely present within the 18-mo thymic epithelium (Figure 3C, Figure S3B: clusters 1, 6, 11,14) and were named as follows: aaTEC1, highly expressing *Wdfc2*, an inducer of epithelial to mesenchymal transition (EMT), which has been previously implicated process in age-related thymic involution; aaTEC2, characterized by expression of *Plet1* and *Cldn3*, markers associated with putative TEC progenitors (Depreter et al., 2008; Hamazaki et al., 2007); aaTEC3, expressing the lipid-droplet accumulation gene *Plin2*; and aaTEC4, identified by their expression of the gene encoding for parathyroid hormone *Pth* (Liu et al., 2010) (Figure 3E, data S5). In addition to these novel TEC populations, we observed the emergence of a new cell subset not corresponding to any of the broader structural cell classifications (Figure 3B and D). This age-associated population expressed both epithelial and mesenchymal markers, EMT regulators, genes linked to G2 cell cycle arrest (*Gadd45a*), the EMT repressor *Ndrg2*, the apoptosis regulator *Bcl2*, and the age-

dependent inflammation-related cytokine *Spp1* (Figure 3F). This transcription profile suggests that this cell population could exist in an intermediary EMT state (Figure 2M) which is notable given the potential for EMT driving thymic aging (Ferrando-Martínez et al., 2015; Gruver et al., 2007). Scatterplots of E-cadherin (*Cdh1*) and vimentin (*Vim*) demonstrate transient expression of selected regulators as cells in this novel population gradually lose their epithelial state and partially gain mesenchymal traits (Figure 3G). These observations suggest that this novel cell type mostly resembles a partial EMT (pEMT) population in concordance with the characteristics of a senescence-associated pEMT identified in kidney fibrosis (Sheng and Zhuang, 2020), without excluding the possibility of some cells fully undergoing EMT (Youm et al., 2009).

Discrete representation of ageing hallmarks in the thymic structural subsets

We coupled pathway with network enrichment analysis to identify pathways associated with age-dependent transcriptional responses. Several pathways associated with aging (López-Otín et al., 2013) were restricted to specific structural cells, such as inflammaging and other intercellular environment alterations (primarily within the mesenchyme), loss of proteostasis and DNA damage (within the TEC compartment), mitochondrial dysfunction (in epithelium and mesenchyme), and ECM disorganization (in epithelium, mesenchyme and endothelium; Figure 3H, data S7). Increased inflammatory responses were evident exclusively in the medFB and med-cmjFB subsets with aging, including increase of the inflammaging-related genes (e.g. *Il6*, *Cxcl1*, *Ccl2*), consistent with recent observations in the aged bone marrow microenvironment (Valletta et al., 2020). We also found that changes in proteostasis pathways were restricted largely to the epithelial compartment, which is notable given the role of proteostasis in aging across many tissues (Hipp et al., 2019). ECs and mesenchymal PCs have an important role in

supporting blood vessel structure and function through juxtacrine or paracrine interactions that regulate vascular permeability and constriction, which are particularly important in the CMJ during the importation of hematopoietic progenitors as well as the export of (soon to be) recent thymic emigrants (Koliaraki et al., 2020; Zachariah and Cyster, 2010). Given these roles in thymus biology, the downregulation of ECM organization pathways in thymic ECs and PCs of 18-mo mice was notable, especially as the cor-cmjFBs, which co-located at the CMJ, also downregulates these same pathways. Downregulation of ECM-related pathways was also observed in TECx and mTEC subsets. Together the biology revealed by these findings may contribute to reduced capacity of the thymus to import hematopoietic progenitors with age (Berent-Maoz et al., 2012). These observations also demonstrate the existence of subset-specific, lineage-specific and lineage-shared responses, characteristic of the thymic structural cell microenvironment with aging (Valletta et al., 2020). These data support recent observations of age-associated changes to be organ-specific and cell lineage specific (The Tabula Muris Consortium, 2020), but extend these findings to organ-specific cell-type subsets.

Differential expression of thymopoietic factors in thymic structural subsets over lifespan

Many key factors have been identified as important for the maintenance or repair of thymic function (Granadier et al., 2021; Velardi et al., 2021), including: the chemokines CXCL12, CCL19, CCL21, and CCL25, which aid in the entry of hematopoietic progenitors into the thymus and the migration of thymocytes within the thymus; Kit ligand, Flt3 ligand, and IL-7, which all act on thymocytes to mediate their differentiation and expansion; and factors such as BMP4, IGF1, GH, KGF (Fgf7), Fgf21, RANKL (Tnfsf11), and VEGFA, which target thymic stromal cells. Expression of thymocyte-acting factors such as Flt3L and IL-7, as well as factors

implicated in TEC regeneration such as BMP4, IGF1, FGF7, and FGF21 decreased globally in older mice (Figure 3I). It was notable that many of these decreases happened within the fibroblast populations. In contrast, factors showing an increased expression with aging include CXCL12 and CCL19 in most of the 18-mo FB subsets, and CCL21A, which was up-regulated in our novel TECx thymic subset (Figure 3I). Upregulation of these chemokines with aging has been observed before (Cané et al., 2012) and might be a compensatory mechanism of the aged thymus for its diminished size and ETP entry.

Delayed endogenous thymic regeneration following acute injury in old mice

Although the thymus is extremely sensitive to injury, and it has endogenous capacity for repair, this regenerative capacity is thought to decline with age, although the mechanisms of this are poorly understood (Granadier et al., 2021). We found that 18-mo mice or older (18-mo+) had delayed recovery of thymic cellularity at day 28 after exposure to a sublethal dose of total body irradiation (SL-TBI) (Figure 4A). Closer kinetic analysis revealed that while 1-2mo mice had fully recovered thymic cellularity after SL-TBI by day 28, aged mice exhibited a significant delay in restoration of cellularity that did not normalize until approximately day 42 (Figure 4B). To assess the extent of damage and repair, we looked at thymic size after damage as a function of baseline cellularity and found that thymi of aged mice did not decline as much as young mice did during the damage phase between days 0 and 4 (Figure 4C). However, restoration of thymic cellularity in the regenerative phase from day 7 was impaired in aged mice (Figure 4C). Flow cytometry analysis on individual subsets revealed only few changes during the damage phase, with a decrease in the return to baseline of mTEC4 and an increase in the return to baseline of capsFB at day 1 (Figure 3D). At the beginning of the repair phase at day 7, we observed few

significant quantitative differences in the regeneration of structural cell subsets of 2-mo or 18-mo+ mice: mTEC3 and mTEC4 demonstrated decreased restoration of cellularity to baseline in aged mice, while arEC, venEC, capsFB, and otherFB all surprisingly exhibited improved restoration of cellularity in aged compared to young mice (Figure 4D).

We reviewed H&E sections for histomorphological changes after damage in 2-mo and 18-mo mice. On day 1 after injury, in both age cohorts there was an extensive depletion of thymocytes and accumulation of cellular debris and granulation tissue formation. While cellular debris was cleared in both age groups, fibrosis, dystrophic calcification and occasional dyskeratotic epithelial cells were observed only in 18-mo mice, suggesting a relative dysfunction in the regenerative process with age (Figure 3E). Using both H&E and immunofluorescence microscopy, days 1 and 4 after damage are both characterized by an overall microanatomical disarray, predominantly evidenced by the loss of distinct demarcation between the cortex and medulla (Figure 4E and F). By day 7, when robust regeneration has been initiated (Wertheimer et al., 2018), there is also lower thymocyte density in old versus young mice (Figure 4E).

To explore the effects of damage and regeneration in structural cells with aging, we analyzed 54,236 $CD45^-$ non hematopoietic stromal cells from day 1, 4 and 7 after SL-TBI, age-matched to the steady state 2-mo and 18-mo populations (Figure 5A to C). We again used canonical markers in conjunction with cell subset gene signatures from 2-mo and 18-mo subsets at steady state to annotate the respective subsets after damage (Figure S5A to I, Figure S6A to I). Despite few compositional changes observed after damage using flow cytometry, analysis of the frequency of cell cycle phases within individual structural cell subsets in the scRNA-seq data (Figure S7A)

revealed a high-proliferating population within the capECs-f that uniquely expressed Apelin (*Apln*). This population expanded on day 7 after damage in the young but not in aged mice (Figure S7B); a similar population of which has been implicated in repair after myeloablative injury in bone marrow (Chen et al., 2019).

To explore if the impaired recovery with age is due to differences in the transcriptional response during the damage (day 1; D1), recovery (day 4; D4) and regeneration (day 7; D7) phase, we selected statistically significant DEGs from all pairwise comparisons (day1, 4 and 7 versus steady state) in the 2-mo subsets and computed enrichment scores per cell in each subset in both age cohorts. All 18-mo FB, MEC and EC subsets showed lesser enrichment scores for the 2-mo DEGs across all phases, with the 18-mo FB subsets to exhibit more consistent lack of response in either direction (up- and down-regulated genes, Figure 5D, Figure S8). Within the TEC compartment, only the mTEC1 subset exhibited enough cells and significant DEGs in all 2-mo comparisons to compute enrichment scores and it consistently showed a lesser enrichment for these DEGs with aging (Figure S8). These observations suggest that the defective response and recovery to acute damage with age could be due to failure of the 18-mo subsets to regulate necessary genes in each of these phases, as compared to the endogenous response in the 2-mo cohort. These findings demonstrate that when looked at globally, the transcriptional responses are diminished with age in a structural cell type-specific manner, with the most activity after damage seen in the 2-mo fibroblast and endothelial populations.

Focusing on the specific pathways that uniquely change during the response to injury in the 2-mo cohort, we found that all FB subsets in 2-mo mice showed up-regulation of pathways related to

immune responses from day 0 to 1, followed by down-regulation of these pathways from day 1 to 4 (Figure 5E). The same subsets also demonstrated a reverse response pattern for genes involved in tissue growth, ECM organization and response to BMP signaling. Notably, the 2-mo PCs demonstrated positive enrichment from day 1 to day 4 (the recovery phase) for pathways related to EC migration and vascular permeability. The above subset and transition-specific responses to irradiation were less profound or fully absent in the old mice. Altogether, transcriptional perturbation caused by acute injury was most pronounced in the 2-mo thymic endothelium and mesenchyme as previously shown for other organs (Krausgruber et al., 2020). With age, transcriptional perturbation diminishes, and programs related to tissue injury are activated at a lower level or not at all in the thymic stroma. Decelerated regeneration in aged tissue may be caused by inability to sense damage preventing the induction of regenerative programs.

We found specific differences in the transcriptional response related to thymopoiesis and thymic regeneration comparing young and aged structural cells (Figure 5F). Notably, expression of BMP4, which we have previously found to be important during the regenerative response after damage (Wertheimer et al., 2018), was increased in young ECs on days 4 and 7 but not in aged ECs. Similarly, expression of the TEC factors IGF1, FGF7 and FGF21, all of which have been implicated in thymic aging or repair, were increased in young mice with no corresponding change in aged mice. Furthermore, we found that the expression of key thymopoietic factors such as Flt3L and KitL increased more in FBs and ECs of young mice on day 1 after damage compared to FBs and ECs from old mice (Figure 5F). Together, these findings suggest that at least part of the decrease in regenerative response with age can be attributed to the attenuation of

the functional response to damage within thymic structural cells.

In summary, these studies offer considerable insight into the age-dependent responses of specific structural cell subsets to acute damage. Furthermore, the data also provide a framework for developing therapeutic strategies to enhance thymic function that can be used to ameliorate periods of lymphopenia and to improve T cell immunity more broadly to aid therapies such as vaccines and cancer immunotherapy.

ACKNOWLEDGEMENTS

We thank Dr. Katia Manova-Todorova, Eric Chan, Radoslaw Junka, Ning Fan, and Afsar Barlas from the Molecular Cytology Core Facility at Memorial Sloan-Kettering Cancer Center for their support and expert advice in the preparation and analysis of immunohistochemistry data.

FUNDING SOURCES

This research was supported by National Institutes of Health award numbers R01-CA228358 (M.R.M.vdB), R01-CA228308 (M.R.M.vdB), R01-HL123340 (M.R.M.vdB), R01-HL147584 (M.R.M.vdB), P01-CA023766 (M.R.M.vdB), R00-CA176376 (J.A.D.), R01-HL145276 (J.A.D.), P01-AG052359 (J.A.D and M.R.M.vdB), and the NCI Cancer Center Support Grants P30-CA015704 (J.A.D.) and P30 CA008748 (M.R.M.vdB). M.R.M.vdB also received support from the Starr Cancer Consortium, the Tri-Institutional Stem Cell Initiative, The Lymphoma Foundation, The Susan and Peter Solomon Divisional Genomics Program, Cycle for Survival, and the Parker Institute for Cancer Immunotherapy. J.A.D received additional support from a Scholar Award from the American Society of Hematology (J.A.D.); the Mechtild Harf (John Hansen) Award from the DKMS Foundation for Giving Life (J.A.D.); the Cuyamaca Foundation (J.A.D.); and the Bezos Family Foundation (J.A.D.). LJ received support from the European Molecular Biology Organization (ALTF-431-2017) and the MSK Sawiris Foundation.

AUTHOR CONTRIBUTIONS

LJ, AIK, EV, JAD, MRMvdB conceived and designed the study. NRM, JAD, MRMvdB acquired funding. LJ, AIK planned research activities. AIK, LS, LJ, LM curated data. AIK, LS, LJ performed initial analysis. AIK, LS, LJ, MS, RS, ALCG provided code and performed computational and statistical analysis of single-cell and bulk RNA-seq data. AIK created the R shiny interactive app. LJ, TJ, EV, KVA, FM analyzed flow cytometric data. AEF performed and analyzed immunofluorescence imaging. KVA analyzed and interpreted H&E sections. LJ, AEF, EV, KVA, JT, AL, KN, NL, FM, HA, SY, MBdS, MD planned and performed experiments. DP, NRM, JAD, MRMvdB supervised study. LJ, AIK, SY, JAD prepared figures and visualized data. LJ, AIK, JAD, MRMvdB wrote the initial draft. All authors reviewed and approved the manuscript.

DECLARATION OF INTERESTS

Dr. Marcel van den Brink has received research support and stock options from Seres Therapeutics and stock options from Notch Therapeutics and Pluto Therapeutics; he has received royalties from Wolters Kluwer; has consulted, received honorarium from or participated in advisory boards for Seres Therapeutics, WindMIL Therapeutics, Rheos Medicines, Merck & Co, Inc., Magenta Therapeutics, Frazier Healthcare Partners, Nektar Therapeutics, Notch Therapeutics, Forty Seven Inc., Priothera, Ceramedix, Lygenesis, Pluto Therapeutics, GlaskoSmithKline, Da Volterra, Vor BioPharma, Novartis (Spouse), Synthekine (Spouse), and Beigene (Spouse); he has IP Licensing with Seres Therapeutics and Juno Therapeutics; and holds a fiduciary role on the Foundation Board of DKMS (a nonprofit organization).

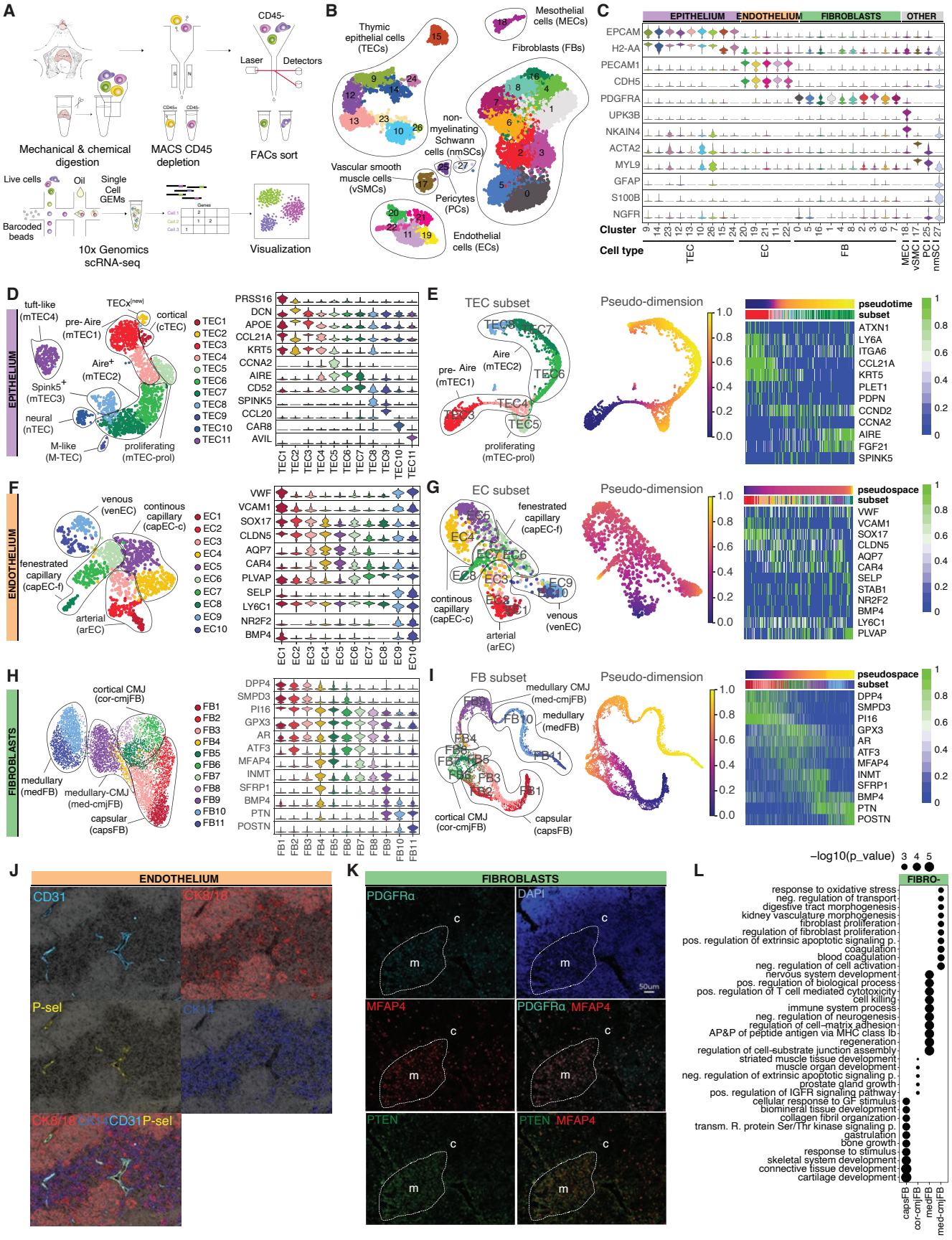
A
Mechanical & chemical digestion
MACS CD45 depletion
CD45-
Laser
Detectors
FACs sort
Live cells
Oil
Single Cell GEMs
Barcoded beads
10x Genomics scRNA-seq
Visualization
B
Thymic epithelial cells (TECs)
Mesothelial cells (MECs)
Fibroblasts (FBs)
non-myelinating Schwann cells (nmSCs)
Vascular smooth muscle cells (vSMCs)
Pericytes (PCs)
Endothelial cells (ECs)
C
EPITHELIUM
ENDOTHELIUM
FIBROBLASTS
OTHER
EPCAM
H2-AA
PECAM1
CDH5
PDGFRA
UPK3B
NKAIN4
ACTA2
MYL9
GFAP
S100B
NGFR
Cluster
Cell type
TEC
EC
FB
MEC
vSMC
PC
nmSC
D
EPITHELIUM
tuft-like (mTEC4)
TECx[new]
pre- Aire (mTEC1)
cortical (cTEC)
Aire+ (mTEC2)
Spink5+ (mTEC3)
neural (nTEC)
M-like (M-TEC)
proliferating (mTEC-prol)
PRSS16
DCN
APOE
CCL21A
KRT5
CCNA2
AIRE
CD52
SPINK5
CCL20
CAR8
AVIL
E
TEC subset
Pseudo-dimension
pseudotime
subset
ATXN1
LY6A
ITGA6
CCL21A
KRT5
PLET1
PDPN
CCND2
CCNA2
AIRE
FGF21
SPINK5
F
ENDOTHELIUM
venous (venEC)
continous capillary (capEC-c)
fenestrated capillary (capEC-f)
arterial (arEC)
VWF
VCAM1
SOX17
CLDN5
AQP7
CAR4
PLVAP
SELP
LY6C1
NR2F2
BMP4
G
EC subset
Pseudo-dimension
pseudospace
subset
VWF
VCAM1
SOX17
CLDN5
AQP7
CAR4
SELP
STAB1
NR2F2
BMP4
LY6C1
PLVAP
H
FIBROBLASTS
cortical CMJ (cor-cmjFB)
medullary (medFB)
medullary-CMJ (med-cmjFB)
capsular (capsFB)
DPP4
SMPD3
PI16
GPX3
AR
ATF3
MFAP4
INMT
SFRP1
BMP4
PTN
POSTN
I
FB subset
Pseudo-dimension
pseudospace
subset
DPP4
SMPD3
PI16
GPX3
AR
ATF3
MFAP4
INMT
SFRP1
BMP4
PTN
POSTN
J
ENDOTHELIUM
CD31
CK8/18
P-sel
CK14
CK8/18 CK14 CD31 P-sel
K
FIBROBLASTS
PDGFRα
DAPI
MFAP4
PDGFRα MFAP4
PTEN
PTEN MFAP4
c
m
50um
L
–log10(p_value)
FIBRO-
response to oxidative stress
neg. regulation of transport
digestive tract morphogenesis
kidney vasculature morphogenesis
fibroblast proliferation
regulation of fibroblast proliferation
pos. regulation of extrinsic apoptotic signaling p.
coagulation
blood coagulation
neg. regulation of cell activation
nervous system development
pos. regulation of biological process
pos. regulation of T cell mediated cytotoxicity
cell killing
immune system process
neg. regulation of neurogenesis
regulation of cell–matrix adhesion
AP&P of peptide antigen via MHC class Ib
regeneration
regulation of cell-substrate junction assembly
striated muscle tissue development
muscle organ development
neg. regulation of extrinsic apoptotic signaling p.
prostate gland growth
pos. regulation of IGFR signaling pathway
cellular response to GF stimulus
biomineral tissue development
collagen fibril organization
transm. R. protein Ser/Thr kinase signaling p.
gastrulation
bone growth
response to stimulus
skeletal system development
connective tissue development
cartilage development
capsFB
cor-cmjFB
medFB
med-cmjFB

Figure 1. Cellular heterogeneity of structural thymic cells in 2-mo mice at steady-state. (**A**) Schematic overview of the experimental approach. (**B**) Uniform manifold approximation and projection (UMAP) of 2-mo CD45- thymic cells labelled by PhenoGraph clusters and main cell types. n_{TOTAL}=10,340 cells. (**C**) Violin plots of canonical markers for main cell types. (**D**, **F** and **H**) UMAPs for epithelial (D), endothelial (F) and fibroblast (H) subsets and assorted violin plots of canonical markers and selected DEGs. (**E**, **G** and **I**) TSNE projection plots for epithelial (E), endothelial (G) and fibroblast (I) subsets labelled by pseudo-temporal ordering. Assorted heatmaps, sorted by pseudo-temporal ordering and labelled by subset, showing marker gene expression gradients. (**J**) IF staining for CD31 (light blue, ECs), P-Selectin (P-sel; yellow, venECs), cytokeratin 8/18 (CK8/18; red, cortex) and cytokeratin 14 (CK14; blue, medulla). (**K**) IF staining for PDGFRα (cyan, FBs), PTN (green, high mRNA expression in medFBs), MFAP4 (red, high mRNA expression in cor-cmjFBs) and DAPI (blue, nucleus). c: cortex, m: medulla. (**L**) Dotplot of top 10 unique pathways per FB group.

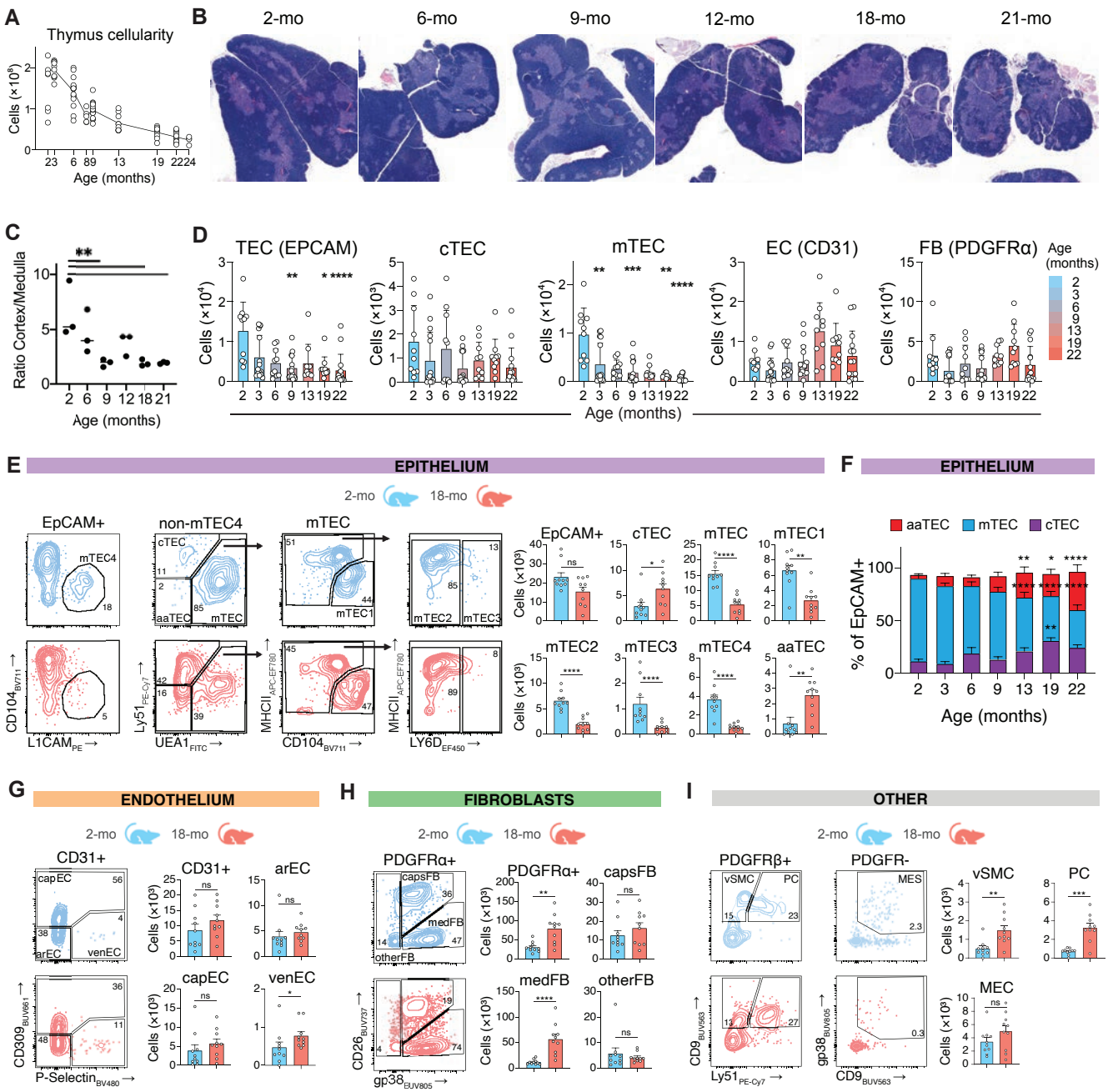
A
Thymus cellularity
Cells (×10⁶)
Age (months)
B
2-mo
6-mo
9-mo
12-mo
18-mo
21-mo
C
Ratio Cortex/Medulla
Age (months)
D
TEC (EPCAM)
cTEC
mTEC
EC (CD31)
FB (PDGFRα)
Cells (×10⁴)
Cells (×10³)
Age (months)
E
EPITHELIUM
2-mo
18-mo
EpCAM+
non-mTEC4
mTEC
cTEC
mTEC4
aaTEC
mTEC1
mTEC2
mTEC3
CD104
L1CAM
Ly51
UEA1
MHCII
LY6D
Cells (×10³)
mTEC4
aaTEC
F
EPITHELIUM
aaTEC
mTEC
cTEC
% of EpCAM+
Age (months)
G
ENDOTHELIUM
2-mo
18-mo
CD31+
capEC
arEC
venEC
CD309
P-Selectin
Cells (×10³)
H
FIBROBLASTS
2-mo
18-mo
PDGFRα+
capsFB
medFB
otherFB
CD26
gp38
Cells (×10³)
I
OTHER
2-mo
18-mo
PDGFRβ+
PDGFR-
vSMC
PC
MES
MEC
CD9
Ly51
gp38
Cells (×10³)

Figure 2. Compositional changes of structural thymic cells with aging. (**A**) Thymic cellularity of female BL6 mice at different ages. (**B** and **C**) Representative hematoxylin and eosin (H&E) stained murine thymi of 2, 6, 9, 12, 18, and 21-month (mo)-old female C57BL/6 mice (B) used to calculate ratio of cortical (dark) to medullary (light) region (C). In (C), each dot represents a biological replicate. (**D**) Flow cytometric analysis of enzyme-digested thymus and absolute cell numbers for major cell types (TECs; cTECs and mTECs; ECs and FBs) in 2, 6, 9, 12, 18, and 21-mo female C57BL/6 mice. (**E, G, H and I**) Flow cytometric analysis of enzyme-digested thymus and assorted quantification (absolute cell numbers and frequencies) for subsets within the TEC (E), EC (G), FB (H) lineages and OTHER cell types (I) in 2-mo (light blue) and 18-mo (light red) female mice. (**F**) Frequency of cTECs, mTECs, and aaTECs among all EpCAM+ thymic epithelial cells. Data combined from 2 independent experiments. *, $p<0.05$; **, $p<0.01$; ***, $p<0.001$; ****, $p<0.0001$.

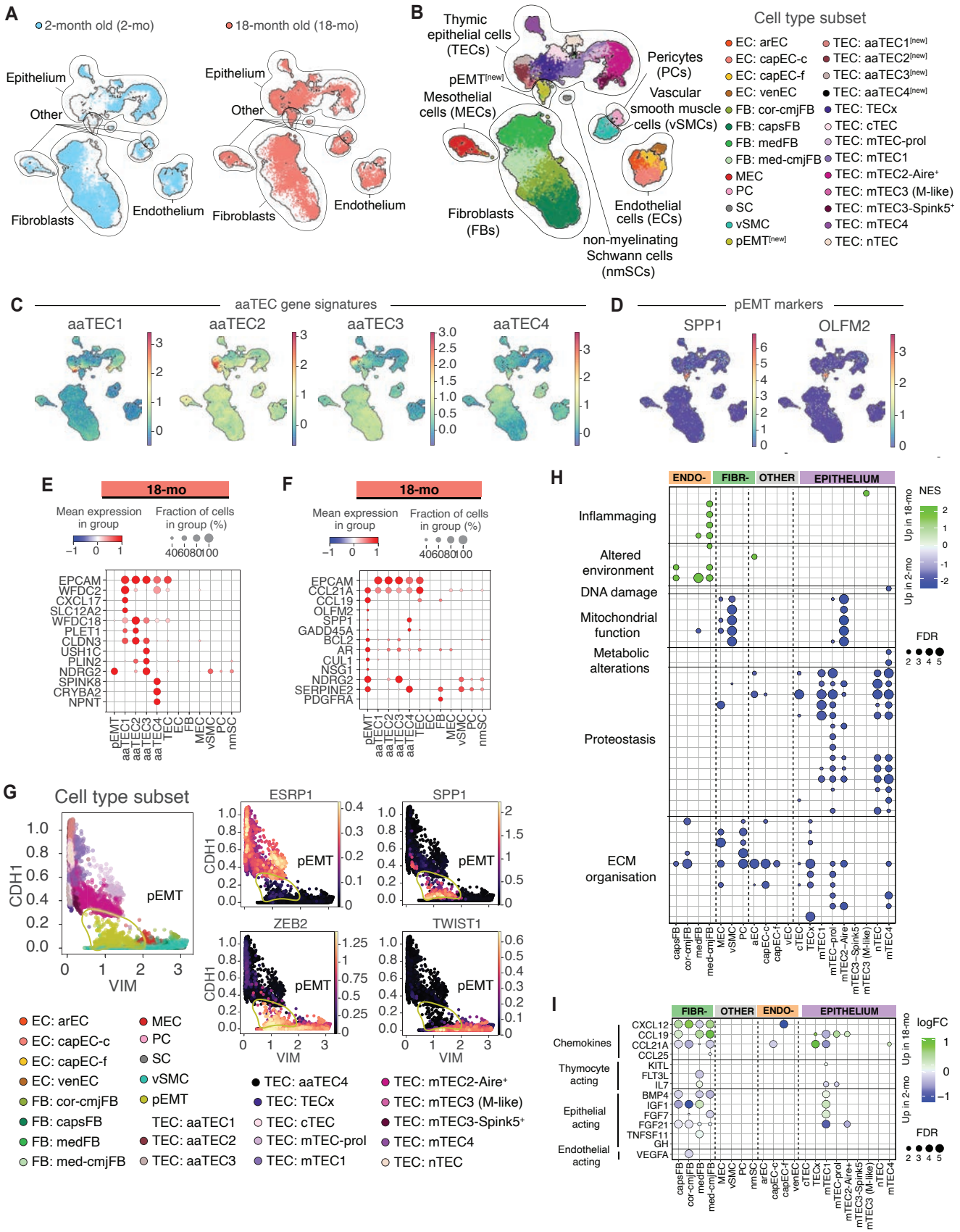
A
2-month old (2-mo)
18-month old (18-mo)
Epithelium
Other
Fibroblasts
Endothelium
B
Thymic epithelial cells (TECs)
pEMT[new]
Mesothelial cells (MECs)
Pericytes (PCs)
Vascular smooth muscle cells (vSMCs)
Fibroblasts (FBs)
Endothelial cells (ECs)
non-myelinating Schwann cells (nmSCs)
Cell type subset
EC: arEC
EC: capEC-c
EC: capEC-f
EC: venEC
FB: cor-cmjFB
FB: capsFB
FB: medFB
FB: med-cmjFB
MEC
PC
SC
vSMC
pEMT[new]
TEC: aaTEC1[new]
TEC: aaTEC2[new]
TEC: aaTEC3[new]
TEC: aaTEC4[new]
TEC: TECx
TEC: cTEC
TEC: mTEC-prol
TEC: mTEC1
TEC: mTEC2-Aire+
TEC: mTEC3 (M-like)
TEC: mTEC3-Spink5+
TEC: mTEC4
TEC: nTEC
C
aaTEC gene signatures
aaTEC1
aaTEC2
aaTEC3
aaTEC4
D
pEMT markers
SPP1
OLFM2
E
18-mo
Mean expression in group
Fraction of cells in group (%)
EPCAM
WFDC2
CXCL17
SLC12A2
WFDC18
PLET1
CLDN3
USH1C
PLIN2
NDRG2
SPINK8
CRYBA2
NPNT
pEMT
aaTEC1
aaTEC2
aaTEC3
aaTEC4
TEC
EC
FB
MEC
vSMC
PC
nmSC
F
18-mo
Mean expression in group
Fraction of cells in group (%)
EPCAM
CCL21A
CCL19
OLFM2
SPP1
GADD45A
BCL2
AR
CUL1
NSG1
NDRG2
SERPINE2
PDGFRA
G
Cell type subset
CDH1
VIM
pEMT
ESRP1
SPP1
ZEB2
TWIST1
EC: arEC
EC: capEC-c
EC: capEC-f
EC: venEC
FB: cor-cmjFB
FB: capsFB
FB: medFB
FB: med-cmjFB
MEC
PC
SC
vSMC
pEMT
TEC: aaTEC1
TEC: aaTEC2
TEC: aaTEC3
TEC: aaTEC4
TEC: TECx
TEC: cTEC
TEC: mTEC-prol
TEC: mTEC1
TEC: mTEC2-Aire+
TEC: mTEC3 (M-like)
TEC: mTEC3-Spink5+
TEC: mTEC4
TEC: nTEC
H
ENDO-
FIBR-
OTHER
EPITHELIUM
Inflammaging
Altered environment
DNA damage
Mitochondrial function
Metabolic alterations
Proteostasis
ECM organisation
NES
Up in 18-mo
Up in 2-mo
FDR
I
FIBR-
OTHER
ENDO-
EPITHELIUM
Chemokines
Thymocyte acting
Epithelial acting
Endothelial acting
CXCL12
CCL19
CCL21A
CCL25
KITL
FLT3L
IL7
BMP4
IGF1
FGF7
FGF21
TNFSF11
GH
VEGFA
logFC
Up in 18-mo
Up in 2-mo
FDR

Figure 3. Transcriptional changes of structural thymic cells with aging. (**A** and **B**) UMAP of 2-mo and 18-mo CD45- thymic cells labelled by age (A) and cell subset (B). nTOTAL=21,359 cells. (**C**) Gene signatures of top 10 DEGs for aaTEC1-4. (**D**) Expression levels of Spp1 and Olfm2. (**E** and **F**) Dotplot of marker genes for aaTEC1-4 (E) and pEMT (F) populations. (**G**) Scatterplots between canonical EMT genes (Cdh1~Vim). Cells colored by cell subset and Esrp1, Spp1, Zeb2 and Twist1 levels. (**H**) Top 5 enriched pathways from 18-mo vs 2-mo subset comparisons grouped by Aging Hallmarks. nmSCs excluded (marginal number of significant DEGs) (see Data S7 for the full list of pathways). (**I**) Fold change of T-cell development and regeneration genes between 18-mo and 2-mo subsets. Circle size: -10log(adj. p-value).

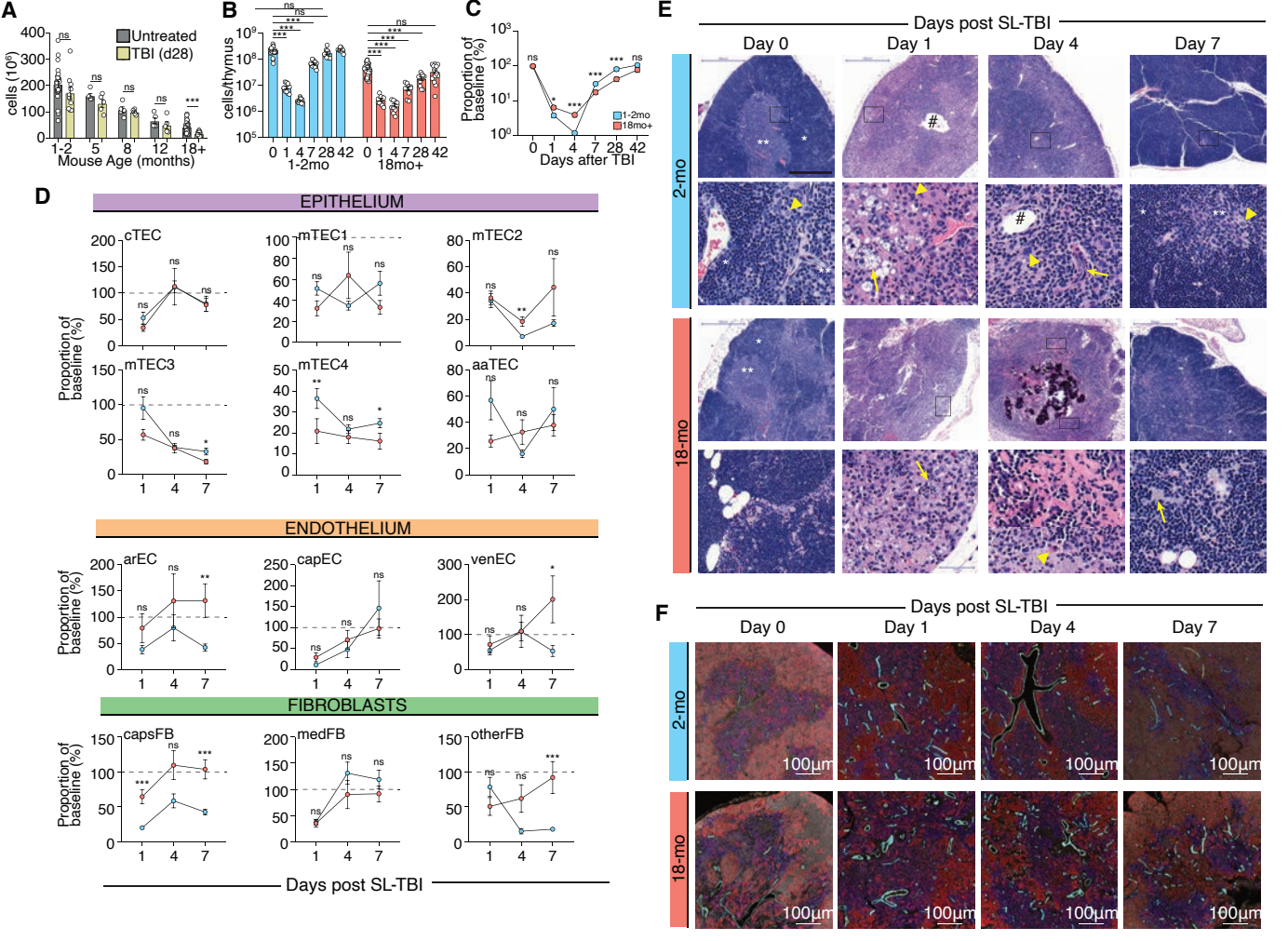
A
cells (10^6)
Untreated
TBI (d28)
Mouse Age (months)
B
cells/thymus
1-2mo
18mo+
C
Proportion of baseline (%)
1-2mo
18mo+
Days after TBI
D
EPITHELIUM
cTEC
mTEC1
mTEC2
mTEC3
mTEC4
aaTEC
ENDOTHELIUM
arEC
capEC
venEC
FIBROBLASTS
capsFB
medFB
otherFB
Proportion of baseline (%)
Days post SL-TBI
E
Days post SL-TBI
Day 0
Day 1
Day 4
Day 7
2-mo
18-mo
F
Days post SL-TBI
Day 0
Day 1
Day 4
Day 7
2-mo
18-mo
100µm

Figure 4. Aging negatively impacts thymic regeneration. (**A** to **C**) Female C57BL/6 mice at the indicated ages were given a sublethal dose of TBI (550cGy) and thymus was assessed at the indicated timepoints. (A and B) Total thymic cellularity. (C) Proportion of total thymic cellularity at the indicated timepoint as a function of steady-state age-matched cellularity. (**D**) Kinetics of recovery for the epithelial, endothelial and fibroblast defined subsets on day 1, 4 and 7 after SL-TBI in 2-mo and 18-mo mice. Cellularity is expressed as a proportion to the cellularity in unirradiated aged-matched controls. Asterisks denote when recovery in either age cohort on a specific timepoint was significantly different to the other cohort. (**E**) Morphologic alterations in the context of acute thymic involution after SL-TBI and thymic reconstitution in 2-mo and 18-mo mice. adipocytes (#), thin cortex (*) (single asterisk), expanded medulla (**). (**F**) IF staining for CD31 (light blue, ECs), P-Selectin (P-sel; yellow, venECs), cytokeratin 8/18 (CK8/18; red, cortex) and cytokeratin 14 (CK14; blue, medulla) at steady-state and at day 1, 4 and 7 after SL-TBI in 2-mo and 18-mo mice.

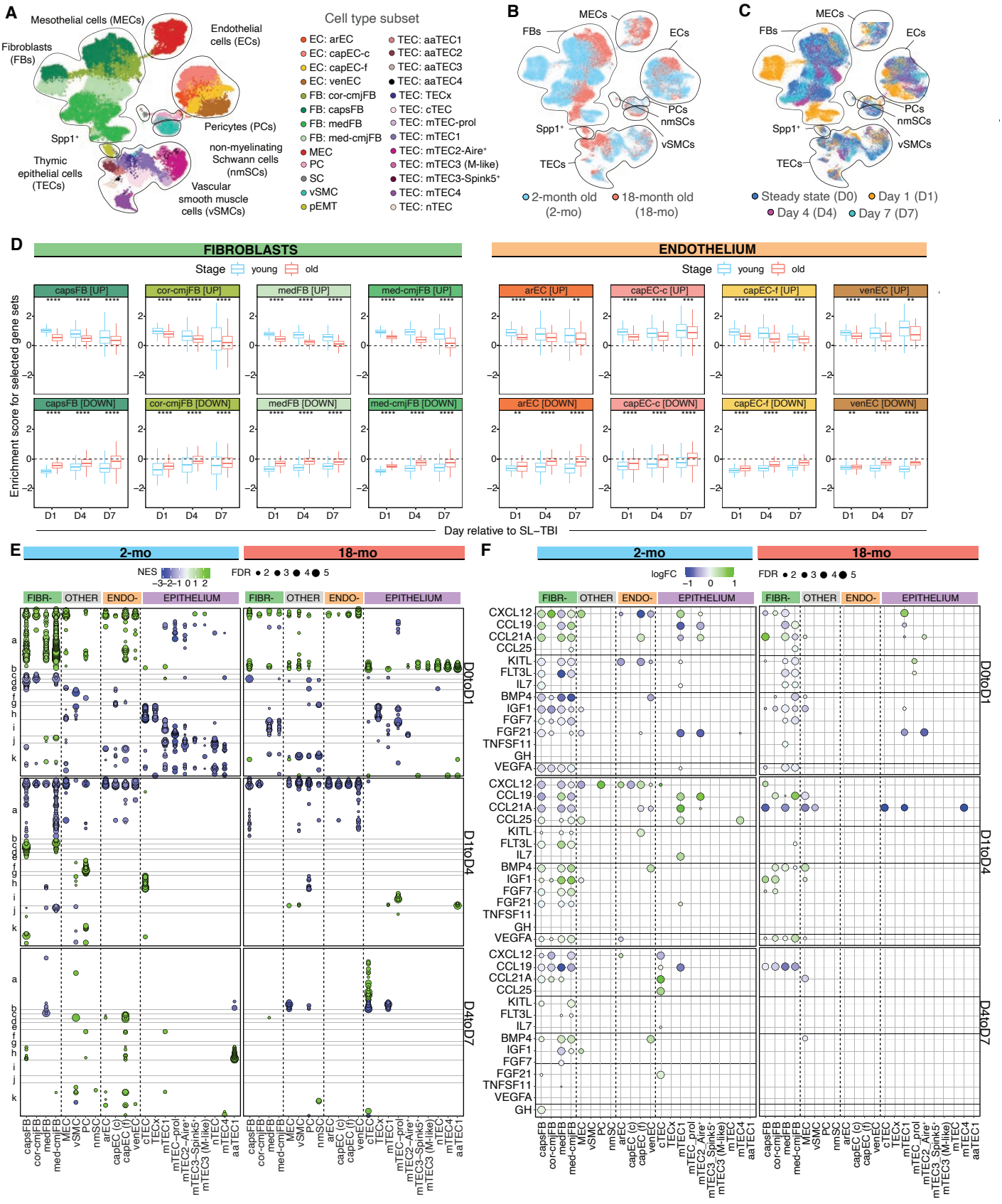
A
Mesothelial cells (MECs)
Endothelial cells (ECs)
Fibroblasts (FBs)
Pericytes (PCs)
Spp1+
non-myelinating Schwann cells (nmSCs)
Thymic epithelial cells (TECs)
Vascular smooth muscle cells (vSMCs)
Cell type subset
EC: arEC
EC: capEC-c
EC: capEC-f
EC: venEC
FB: cor-cmjFB
FB: capsFB
FB: medFB
FB: med-cmjFB
MEC
PC
SC
vSMC
pEMT
TEC: aaTEC1
TEC: aaTEC2
TEC: aaTEC3
TEC: aaTEC4
TEC: TECx
TEC: cTEC
TEC: mTEC-prol
TEC: mTEC1
TEC: mTEC2-Aire+
TEC: mTEC3 (M-like)
TEC: mTEC3-Spink5+
TEC: mTEC4
TEC: nTEC
B
MECs
FBs
ECs
PCs
nmSCs
Spp1+
vSMCs
TECs
2-month old (2-mo)
18-month old (18-mo)
C
MECs
FBs
ECs
PCs
nmSCs
Spp1+
vSMCs
TECs
Steady state (D0)
Day 1 (D1)
Day 4 (D4)
Day 7 (D7)
D
FIBROBLASTS
ENDOTHELIUM
Stage young old
capsFB [UP]
cor-cmjFB [UP]
medFB [UP]
med-cmjFB [UP]
arEC [UP]
capEC-c [UP]
capEC-f [UP]
venEC [UP]
capsFB [DOWN]
cor-cmjFB [DOWN]
medFB [DOWN]
med-cmjFB [DOWN]
arEC [DOWN]
capEC-c [DOWN]
capEC-f [DOWN]
venEC [DOWN]
Enrichment score for selected gene sets
D1 D4 D7
Day relative to SL−TBI
E
2-mo
18-mo
NES
FDR
FIBR-
OTHER
ENDO-
EPITHELIUM
D0toD1
D1toD4
D4toD7
F
2-mo
18-mo
logFC
FDR
CXCL12
CCL19
CCL21A
CCL25
KITL
FLT3L
IL7
BMP4
IGF1
FGF7
FGF21
TNFSF11
GH
VEGFA
D0toD1
D1toD4
D4toD7

Figure 5. Magnitude of transcriptional perturbation following irradiation is attenuated in aged thymic stroma. (**A** to **C**) UMAPs of 2-mo and 18-mo CD45- thymic cells at steady state and at d1, d4 and d7 after SL-TBI, labelled by cell type subset (A), age (B) and day after SL-TBI (C). (**D**) Boxplots showing the MAST enrichment scores for up- and down-regulated genes based on the 2-mo day 1 (D1), day 4 (D4) and day 7 (D7) comparisons to steady-state (D0) for all endothelial and fibroblast subsets. (**E**) Enriched pathways from all transition comparisons (d1-d0, d4-d1, d7-d4) for each subset per age cohort, categorized under major biological processes. a: Immune response, b: Peptidase activity, c: ECM organization, d: Response to BMP signaling, e: Tissue growth, f: EC migration - Vascular permeability, g: Cellular respiration, h: Spliceosome, i: Proteostasis and j: Various (see Data S8 for the full list of pathways). (**F**) Fold change of T-cell development and regeneration genes in all transition comparisons (d1-d0, d4-d1, d7-d4) per age cohort for each subset. Circle size: -10log(adj. p-value).

METHODS

Isolation of CD45-negative thymic cells for single-cell RNA sequencing

All steps were performed at 4 C unless indicated. 10-15 thymi of 2-month-old or 18-month-old female C57BL/6 mice were excised and enzymatically digested following and adapted protocol (Gray et al., 2008; Jain and Gray, 2014). Briefly, thymi were mechanically dissociated into ca. 2 mm pieces. Tissue pieces were incubated with a digestion buffer (RPMI, 10% FCS, 62.5 um/mL liberase TM, 0.4 mg/ml DNase I) twice for 30 min at 37 C. Between incubation steps, supernatant containing dissociated cells was transferred to 50 mL conical tubes equipped with 100 um filter. Cells were pelleted by centrifugation at 400g for 5 min. Cell pellets were incubated with anti-mouse CD45 microbeads and CD45-positive cells were depleted from cell suspension using magnetic-associated cell sorting (MACS) on LS columns according to manufacturer's protocol. Following red blood cell lysis using ACK buffer, the CD45-depleted cell fraction was incubated with an antibody cocktail for 15 min at 4 C and cells of interest were purified by fluorescent-associated cell sorting (FACS) on a BD Biosciences Aria II using a 100 um nozzle. Cells were sorted into tubes containing RPMI supplemented with 2% BSA. FACS-purified cells were spun down at 400g for 5 min and resuspended in PBS supplemented with 0.04 % BSA for generation of single-cell suspensions.

Generation of single-cell suspensions

The single-cell RNA-Seq of FACS-sorted cell suspensions was performed on Chromium instrument (10X genomics) following the user guide manual (CG00052 Rev E) and using Single

Cell 3' Reagent Kit (v2). The viability of cells prior to loading onto the encapsulation chip was 73-98%, as confirmed with 0.2% (w/v) Trypan Blue stain. Each sample, containing approximately 8000 cells, was encapsulated in microfluidic droplets at a final dilution of 66–70 cells/µl (a multiplet rate ~3.9%). Following reverse transcription step the emulsion droplets were broken, barcoded-cDNA purified with DynaBeads and amplified by 12-cycles of PCR: 98℃ for 180 s, 12x (98℃ for 15 s, 67˚C for 20 s, 72℃ for 60 s), and 72℃ for 60 s. The 50 ng of PCR-amplified barcoded-cDNA was fragmented with the reagents provided in the kit, purified with SPRI beads and resulting DNA library was ligated to the sequencing adapter followed by indexing PCR: 98℃ for 45 s; 12x 98℃ for 20 s, 54℃ for 30 s, 72℃ for 20 s), and 72℃ for 60 s. The final DNA library was double-size purified (0.6–0.8X) with SPRI beads and sequenced on Illumina Nova-Seq platform (R1 – 26 cycles, i7 – 8 cycles, R2 – 70 cycles or higher) at depth of 200-270 million reads per sample.

Immunohistochemistry

Paraffin-embedded tissue sections were cut at 5 µm and heated at 58°C for 1 hr. Samples were pretreated with EDTA-based epitope retrieval ER2 solution (Leica, AR9640) for 20 mins. at 95°C. The antibodies: P-Selectin (LS Bio, Cat # LS-B3578, 2.5 ug/ml), CD31 (Abcam, Cat # ab182981, 0.016ug/ml), Cytokeratin 14 (Abcam, Cat# ab7800, 1ug/ml), Cytokeratin 8/18 (Abcam, Cat# ab53280, 0.12 ug/ml) were detected in sequence with Leica Bond RX. Appropriate species- matched secondary antibodies and Leica Bond Polymer anti-rabbit HRP

were used, followed by Alexa Fluor tyramide signal amplification reagents (Life Technologies, B40953, B40958) and CF® dye tyramide conjugates (Biotium, 92172, 92174).

After staining, slides were washed in PBS and incubated in 5 µg/ml 4',6-diamidino-2-phenylindole (DAPI) (Sigma Aldrich) in PBS (Sigma Aldrich) for 5 min, rinsed in PBS, and mounted in Mowiol 4–88 (Calbiochem). Slides were kept overnight at -20°C before imaging.

Thymuses were dissected and placed in 4% paraformaldehyde (PFA) for two hours. After fixation, thymuses were washed with 1XPBS, placed in 20% sucrose/1XPBS, and incubated overnight at 4°C. Thymuses were embedded in OCT before snap-freezing on dry ice and kept at -80°C before utilizing them for sectioning. We generated 10µm thick sections using a Leica CM 3050S cryostat and blocked tissue sections with blocking buffer for 30-minutes at room temperature. The blocking buffer consisted of 1XPBS supplemented with 0.5% BSA, 10% donkey serum, and 0.2% Tween 20. We prepared a primary antibody mix in blocking buffer. We incubated tissue sections with primary antibody mix for 2-hours at room temperature in a humid chamber. After primary antibody staining, we washed sections with 1XPBS and incubated them with secondary antibody solution for 30-minutes, protected from light in a humid chamber. The secondary antibody mix was prepared using blocking buffer. We washed with 1XPBS and stained with DAPI/1XPBS solution for 5-minutes. We washed with dH2O and mounted coverslips with Fluorogel mounting media (ElectronMicroscopy Sciences, Cat. 17985-10).

The primary antibodies used were anti-PTN (Goat Pleiotrophin polyclonal antibody, MyBioSource, MBS423578), anti-MFAP4 (Rabbit MFAP4 polyclonal antibody, Invitrogen, PA5-24865), anti-PDGFRα (Rat CD140a polyclonal antibody, BioLegend, Cat. 135902).

The secondary antibodies used were Alexa Fluor® 647 donkey anti-rabbit IgG (H+L) (Invitrogen, Cat. A31573), Alexa Fluor 488-conjugated AffiniPure Donkey Anti-Chicken IgYtt (IgG) (Jackson ImmunoResearch Laboratories, Cat.703-545-155), and Alexa Fluor® 594 donkey anti-rat IgG (Invitrogen, Cat.A21209).

CD45- single cell RNA-seq preprocessing and downstream data analysis

Quality control, de-multiplexing, alignment and quantification. To construct a count matrix the FASTQ files were processed using the Sequence Quality Control (SEQC) package (Azizi et al., 2018), which also included de-multiplexing, alignment, error correction and the generation of a raw digital expression matrix by collapsing groups of reads with the same UMI, cell barcode and gene annotation. Viable cells were identified on the basis of library size; whereby cells were filtered beyond the knee point of the second derivative of the empirical cumulative density function of total cell transcript counts. Cells with low complexity libraries were filtered out. Cells with >20% of transcripts derived from mitochondria were excluded. Genes detected in fewer than ten cells or genes with low expression levels were also excluded. After filtering and barcode correction the average reads per single-cell were approximately 54.176,08, and median reads per transcript was 7.97. A median library size of 4,199 transcripts per cell was retained for downstream analyses.

Gene filtering and library size normalization. The SEQC-generated count matrices were processed with the scanpy(Wolf et al., 2018) toolkit. Ribosomal genes and genes that were not expressed in any cell were removed from downstream analysis. Each cell was then normalized to

a total library size of 10,000 reads and gene counts were log-transformed using the log(X+1) formula, in which log denotes the natural logarithm.

Dimension reduction and unsupervised clustering analysis. Principal component analysis was applied to reduce noise prior to data clustering. To select the optimal number of principal components to retain for each dataset, the knee point (eigenvalues smaller radius of curvature) was used. Phenograph(Levine et al., 2015) was used to identify clusters within the PCA-reduced data. An adjusted Rand score (range: 5-150, step: 5) higher or equal to 0.8 for 4 consecutive steps was used to select a robust nearest neighbor parameter (k) for Phenograph.

Removal of doublets, contaminants and bad quality cells

Doublets. Doublets were predicted by the DoubletDetection(Gayoso and Shor, 2020) python package using the version 2.4.0 suggested parameters for the classifier (use_phenograph=True, verbose=True, standard_scaling=False) and specifying p_thresh=1e-7 and voter_thresh=0.8 as threshold values. The raw counts of each individual sample were used as input.

Contaminating cells. Although cells were negatively sorted prior to sequencing for the CD45 marker, a small amount of CD45+ cells (expressing the *Ptprc* gene) was detected and marked as contaminating in our scRNA-seq data.

Bad quality cells. Quality of the single cells was computationally assessed based on total counts, number of genes, mitochondrial fraction and ribosomal fraction per cell, with low total counts, low number of genes (≤1000) and high mitochondrial content (≥0.2) as negative indicators of cell quality. Cells characterized by more than one negative indicator were considered as “bad” quality cells.

To remove in an unbiased way contaminants and bad quality cells, we assessed them in a cluster basis rather than individually. PhenoGraph-generated clusters with a “bad” quality profile and/or a high number of contaminating cells (expressing high levels of *Ptprc*) were removed on a per sample basis. Additionally, cells marked as doublets were filtered out. Overall, a total of 24,705 cells (doublets, CD45+, bad quality), representing 24.6% of all our scRNA-seq data, was excluded from further analysis (see Figure S10 for per sample metrics). After removal of these cells, PCA and unsupervised clustering analysis was reapplied to the filtered data as described in the Methods section above.

Pseudo-temporal ordering of cells within each structural compartment

Cells were aligned along continuous cell state trajectories (pseudotemporal ordering) using Palantir(Setty et al., 2019). The *palantir.utils.run_diffusion_maps* function was employed to generate the diffusion maps of the selected populations (2-mo EC, FB and TEC subsets at steady state) as an estimate of the phenotypic manifold for the top 5 principal components (low dimension) of each population. The resulting diffusion maps were visualized using a tSNE projection.

Differential expression analysis

Differential expression analysis between the PhenoGraph-generated clusters was performed using MAST (Finak et al., 2015) with default parameters, except for the comparisons between timepoints where both day and stage of the dataset was incorporated within the hurdle model. In all cases, differentially expressed genes were considered statistically significant if the FDR-adjusted p-value was less than 0.05 and the absolute value of the $\log_2$(fold change) was greater or equal to 1.25.

Generation of cell type/subset-specific gene signatures

To select maximally specific genes per cell type/subset, we ran MAST for all pairwise cluster comparisons (each versus the rest) and retained the top 10 DEGs for a given cluster (FDR<=0.05, sorted by decreasing coef). To generate the unique cluster signatures per se, we used the *sc.tl.score_genes()* function from *scanpy* (Wolf et al., 2018) that calculates averaged scores based on the cluster specific genes (scores are subtracted with a randomly sampled reference gene set).

Mapping of 2-month-old steady state thymic populations onto the steady state thymic subsets of 18-month-old mice

We applied unsupervised clustering analysis with Phenograph to identify clusters in the 18-mo steady state dataset and used canonical markers that marked existing cell types in the 2-mo thymic stroma to identify those same populations within the 18-mo cohort (see Figure S3). We subsetted and reanalyzed the 18-mo EC, FB and TEC subsets in a similar fashion we did for the 2-mo dataset and re-computed clusters within these cell types using PhenoGraph. We then used *de novo* gene signatures from the 2-mo EC and TEC subsets (top 10 DEGs, MAST: FDR<=0.05 & sorted in descending order by coef, Supplementary Files 2, 3) to map all PhenoGraph-generated clusters within each cell type to the ones present in the 2-mo cohort and 4 prominent FB markers (*Pi16*, *Gpx3*, *Serpine2* and *Des*, Supplementary File 4) whose absence or presence define consistently the 4 main FB subsets within the young thymus. This allowed us to map and compare cell types and subsets from the two different age cohorts in an unbiased way (see Figure S3).

Mapping steady state subsets onto the SL-TBI timeseries dataset within each age cohort

To identify the steady state cell types and subsets within the EC, FB and TEC populations after irradiation we again subsetted and reanalyzed our datasets as described here. Due to the limited number of cells in some of the aged and irradiated subsets we applied unsupervised clustering analysis on all samples combined per age cohort and assigned cell identities using (a) canonical markers for the major cell types, (b) steady state gene signatures from 2-mo and 18-mo TEC and EC subsets for the combined 2-mo and 18-mo TEC and EC time series data respectively (top 10 DEGs, MAST: FDR<=0.05 & sorted in descending order by coef, Supplementary Files 2-3, 5-6, Figure S4 and S5) and (c) the 4 prominent FB markers (*Pi16*, *Gpx3*, *Serpine2* and *Des* for the combined 2-mo and 18-mo FB time series data respectively. Once annotated, we combined the 2-mo and 18-mo time series datasets in one UMAP (Figure 4b).

Pathway enrichment analysis

Pathway enrichment analysis was performed with gProfiler(Reimand et al., 2007) or GSEA (Subramanian et al., 2005) according to the gene list and rank metric provided.

GSEA. The GSEA Preranked module was used to predict pathway enrichment in threshold free comparisons: (a) 18-mo vs 2-mo subsets at steady state and (b) day transition comparisons per subset within each age cohort (e.g. day 1 vs steady state, day 4 vs day 1 and day 7 vs day 4 comparisons of the 2-mo venEC subset). We created rankings for all differentially expressed genes by multiplying the -*log*10 adj. P val with the sign of the coefficient value (log-transformed fold change) generated by the differential expression analysis with MAST. When the adj. P val for a particular gene was zero, it was subsetted by the next smallest adj P value in the specific comparison to avoid the resulting log-transformed value to be set to infinite. If more than one adj P val were zero, after subsetting the value by the next smallest adj. P value we used the *jitter ()*

function in *R* to add a small amount of noise to each value and then sorted the resulting values in a decreasing way based on their |coef| value. Predicted pathways with an FDR<=0.05 were considered as significantly enriched.

gProfiler. The *gProfiler2*(Raudvere et al., 2019) R package was used to predict enriched pathways for the 2-mo FB subsets and the novel TEC2 subset at steady state. DEG lists were generated by comparing each 2-mo FB/TEC subset versus the rest of the 2-mo FB/TEC subsets at steady state respectively using MAST. MAST-generated DEG lists were next sorted by coef value and filtered for an adj. P value <= 0.05 and coef>=0.585.

Network analysis

Network analysis of the significantly enriched GSEA pathways from comparisons of interest was performed using the Cytoscape(Shannon et al., 2003) module EnrichmentMap(Merico et al., 2010). We used EnrichmentMap to organize enriched pathways (FDR<=0.05) with a high overlap of genes (default cutoff similarity: 0.375) in the same network allowing for a simplified and intuitive visualization of the distinct processes that are significantly represented in the subset/stage and day transitions of interest. This facilitated interpretation of the enriched pathways from the plethora of comparisons and allowed categorization of all resulting pathways into networks based on the overlap of the genes contributing to the pathways enrichment. Manual inspection of the resulting networks allowed allocation of network-related annotations. Individual pathways that were not part of an existing network were manually annotated to the existing categories based on their biological function or grouped under “other”.

Cell cycle phase assignment

To attribute the cell cycle phase to each cell we used the *sc.tl.score_cell_cycle_genes()* function from *scanpy*(Wolf et al., 2018) that calculates averaged scores from curated sets of genes (scores were subtracted with a randomly sampled reference gene set) for the S and G2/M phase separately. To define the S and G2/M associated gene lists we used a core set of 97 cell cycle related genes(Tirosh et al., 2016) (S phase: 43 genes, G2/M phase: 54 genes; mapped to mouse orthologs). Cells not assigned to either S or G2/M phase were considered to belong to G1 phase.

CD45- bulk RNA-seq preprocessing and downstream data analysis

Quality control, alignment and gene count quantification. Quality control (QC) of the raw read files (FASTQ) was performed using the FastQC(Andrews, 2010) tool. Low quality reads and adapter contaminants were removed using Trimmomatic(Bolger et al., 2014) (default parameters for paired-end reads) and post-trimmed reads were re-assessed with FastQC to verify adapters removal and potential bias introduced by trimming. QC-approved reads were aligned to the GRCm38.p5 (mm10) mouse genome assembly (GENCODE; M12 release) with STAR(Dobin et al., 2013) aligner using default parameters and --*runThreadN* set to 32 to increase execution speed. The STAR-aligned files were then used as input to the featureCounts(Liao et al., 2014) tool (default parameters) to quantify gene expression levels and construct the count matrix.

Low gene count removal and library size normalization. The raw count matrix was converted to a DGEList object in R using the *readDGE()* function from the edgeR(Robinson et al., 2010) package. Lowly expressed genes were removed using the *filterByExpr()* function for the groups of interest prior to comparison with the scRNA-seq datasets.

Bulk RNA-seq vs scRNA-seq. scRNA-seq sample reproducibility was verified using bulk RNA-seq data for the CD45- sorted populations. Comparison between bulk and single cell RNA-seq

CD45- transcriptional profiles was performed by computing Pearson's correlation between log_{10}-transformed raw bulk counts (per biological replicate) and $\log_{10}$-transformed averaged raw single cell counts (per technical replicate) for the relevant datasets across the SL-TBI timeframe (Figure S10).

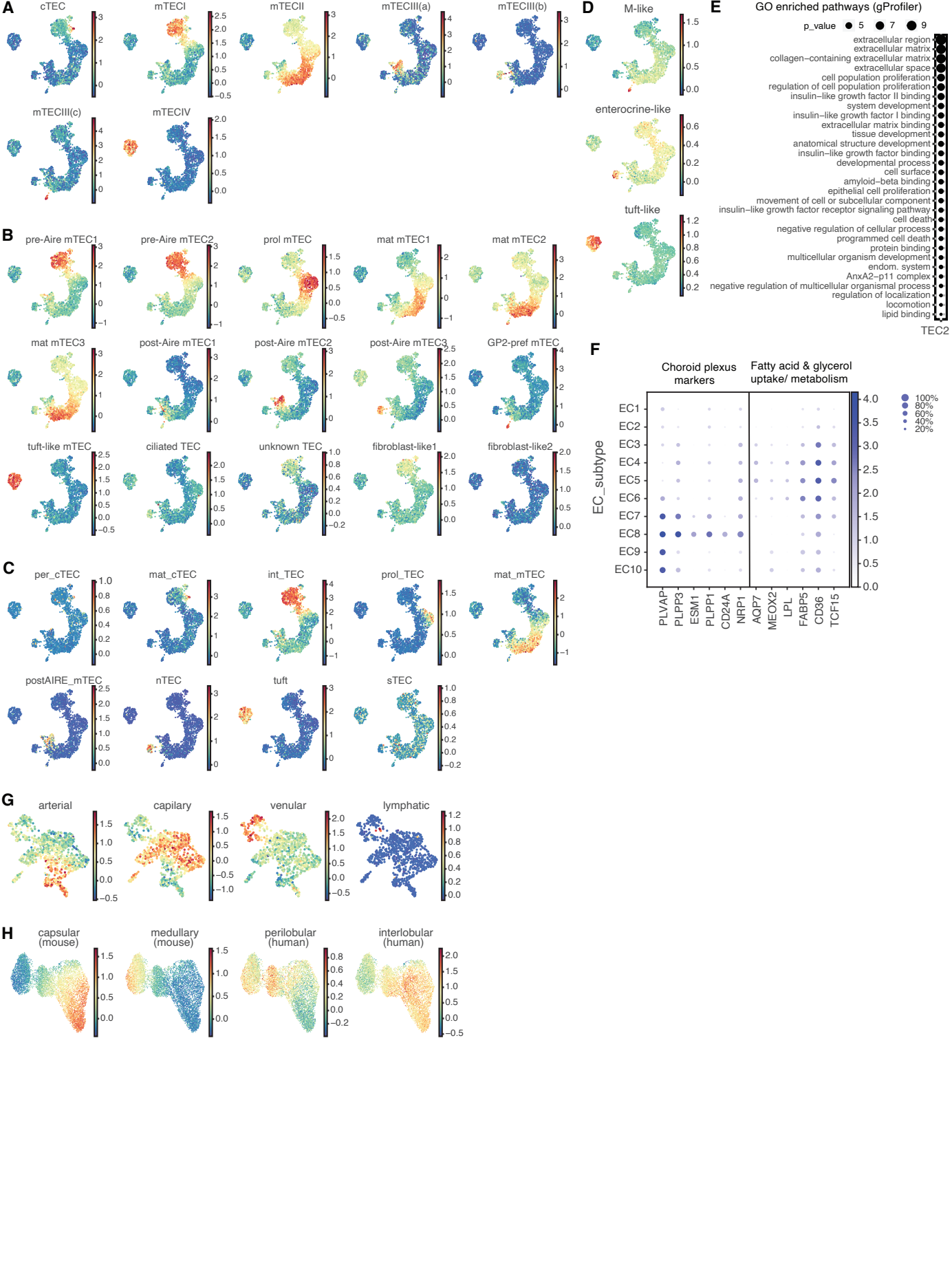
A
cTEC
mTECI
mTECII
mTECIII(a)
mTECIII(b)
mTECIII(c)
mTECIV
B
pre-Aire mTEC1
pre-Aire mTEC2
prol mTEC
mat mTEC1
mat mTEC2
mat mTEC3
post-Aire mTEC1
post-Aire mTEC2
post-Aire mTEC3
GP2-pref mTEC
tuft-like mTEC
ciliated TEC
unknown TEC
fibroblast-like1
fibroblast-like2
C
per_cTEC
mat_cTEC
int_TEC
prol_TEC
mat_mTEC
postAIRE_mTEC
nTEC
tuft
sTEC
D
M-like
enterocrine-like
tuft-like
E
GO enriched pathways (gProfiler)
p_value
5
7
9
extracellular region
extracellular matrix
collagen−containing extracellular matrix
extracellular space
cell population proliferation
regulation of cell population proliferation
insulin−like growth factor II binding
system development
insulin−like growth factor I binding
extracellular matrix binding
tissue development
anatomical structure development
insulin−like growth factor binding
developmental process
cell surface
amyloid−beta binding
epithelial cell proliferation
movement of cell or subcellular component
insulin−like growth factor receptor signaling pathway
cell death
negative regulation of cellular process
programmed cell death
protein binding
multicellular organism development
endom. system
AnxA2−p11 complex
negative regulation of multicellular organismal process
regulation of localization
locomotion
lipid binding
TEC2
F
Choroid plexus markers
Fatty acid & glycerol uptake/ metabolism
EC_subtype
EC1
EC2
EC3
EC4
EC5
EC6
EC7
EC8
EC9
EC10
PLVAP
PLPP3
ESM1
PLPP1
CD24A
NRP1
AQP7
MEOX2
LPL
FABP5
CD36
TCF15
100%
80%
60%
40%
20%
G
arterial
capilary
venular
lymphatic
H
capsular (mouse)
medullary (mouse)
perilobular (human)
interlobular (human)

Figure S1. Characterization of the 2-mo epithelial, endothelial and fibroblast populations at steady-state. (**A-C**) UMAPs of 2-mo TEC subsets labelled by gene signatures for TEC subsets from known literature (see Supplementary Table # and Supplementary File #). (**D**) UMAPs of 2-mo TEC subsets (Figure 1d) labelled by gene signatures for M, tuft and enterocrine epithelial subsets from the small intestine (Supplementary File #). (**E**) Top 30 enriched GO pathways for 2-mo TEC subsets (Methods, gProfiler, MAST; coef>=1.5, FDR<=0.05). (**F**) UMAP plots of 2-mo EC subsets (Figure 1E) labelled by gene signatures for conserved vascular bed types from multiple organ ECs (Supplementary File #). (**G**), Dotplot of 2-mo EC subsets (Figure 1e) showing gene expression levels and coverage for markers coexpressed in EC subsets in other organs. (**H**) Top 30 enriched GO pathways for novel 2-mo EC subsets (Methods, gProfiler, MAST; coef>=1.5, FDR<=0.05). (I) UMAPs of 2-mo FB subsets (Figure 1f) labelled by gene signatures for extracellular matrix compartments (perilobular/interlobular and capsular/medullary, Supplementary File #).

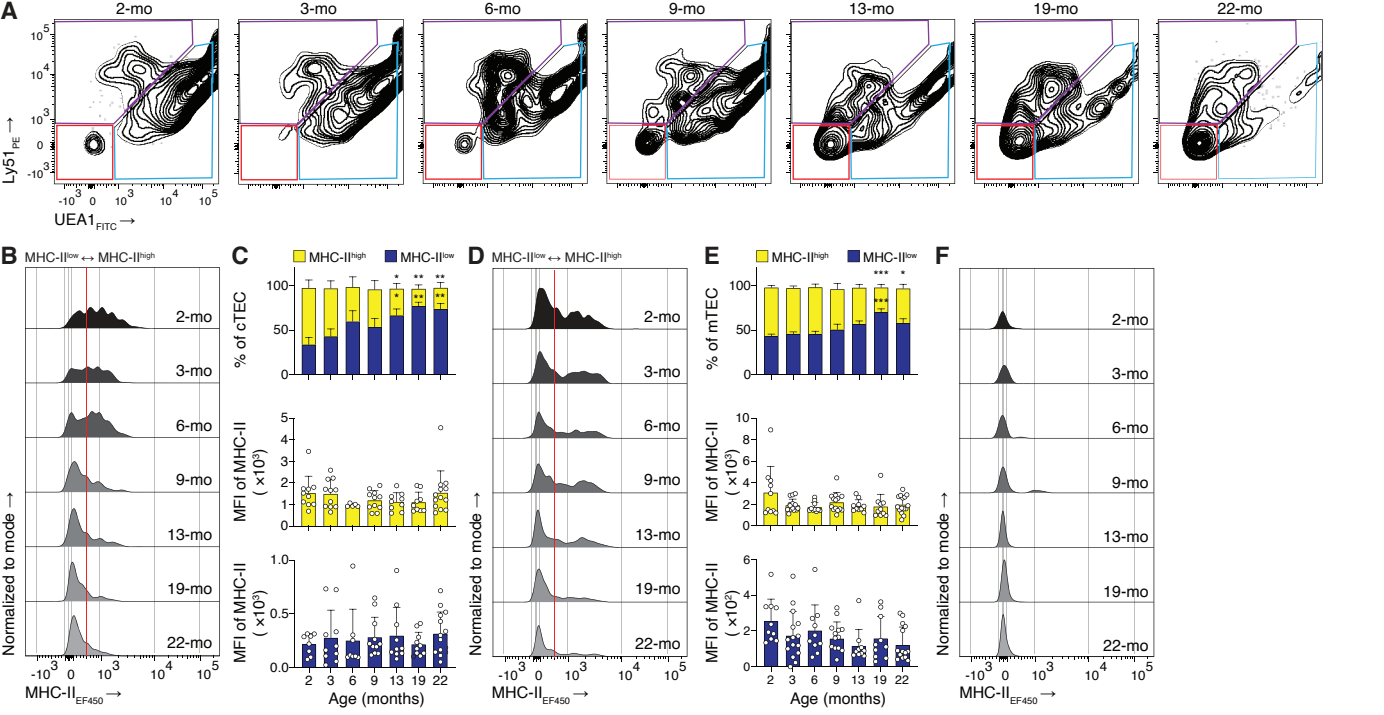
A
2-mo
3-mo
6-mo
9-mo
13-mo
19-mo
22-mo
Ly51PE →
UEA1FITC →
B
MHC-IIlow ↔ MHC-IIhigh
Normalized to mode →
MHC-IIEF450 →
C
MHC-IIhigh
MHC-IIlow
% of cTEC
MFI of MHC-II (×10³)
Age (months)
D
MHC-IIlow ↔ MHC-IIhigh
E
MHC-IIhigh
MHC-IIlow
% of mTEC
MFI of MHC-II (×10³)
MFI of MHC-II (×10²)
Age (months)
F

Figure S2. Compositional changes among thymic epithelium with age. (**A**) Flow cytometric analysis of enzyme-digested murine thymus of female mice of indicated ages. Plots show cells gated on single/live/TER119-/CD45-/EpCAM+/MHCII+ cells. Purple gate marks Ly51+/UEA1-low cortical TECs (cTEC), blue gate marks Ly51-low/UEA1+ medullary TECs, red gate marks Ly51-/UEA1- age-associated TECs. (**B**) Histograms show MHC-II expression among cTECs with red line indicating MHC-II low and high subsets. (**C**) Frequency of MHC-II low and high cTECs among all cTECs, and expression of MHC-II among cTEC-high and low subsets is shown. (**D**) Histograms show MHC-II expression among mTECs with red line indicating MHC-II low and high subsets. (**E**) Frequency of MHC-II low and high mTECs among all mTECs, and expression of MHC-II among mTEC-high and low subsets is shown. (**F**) Histograms show MHC-II expression of aaTECs. *, $p<0.05$; **, $p<0.01$; ***, $p<0.001$; ****, $p<0.0001$.

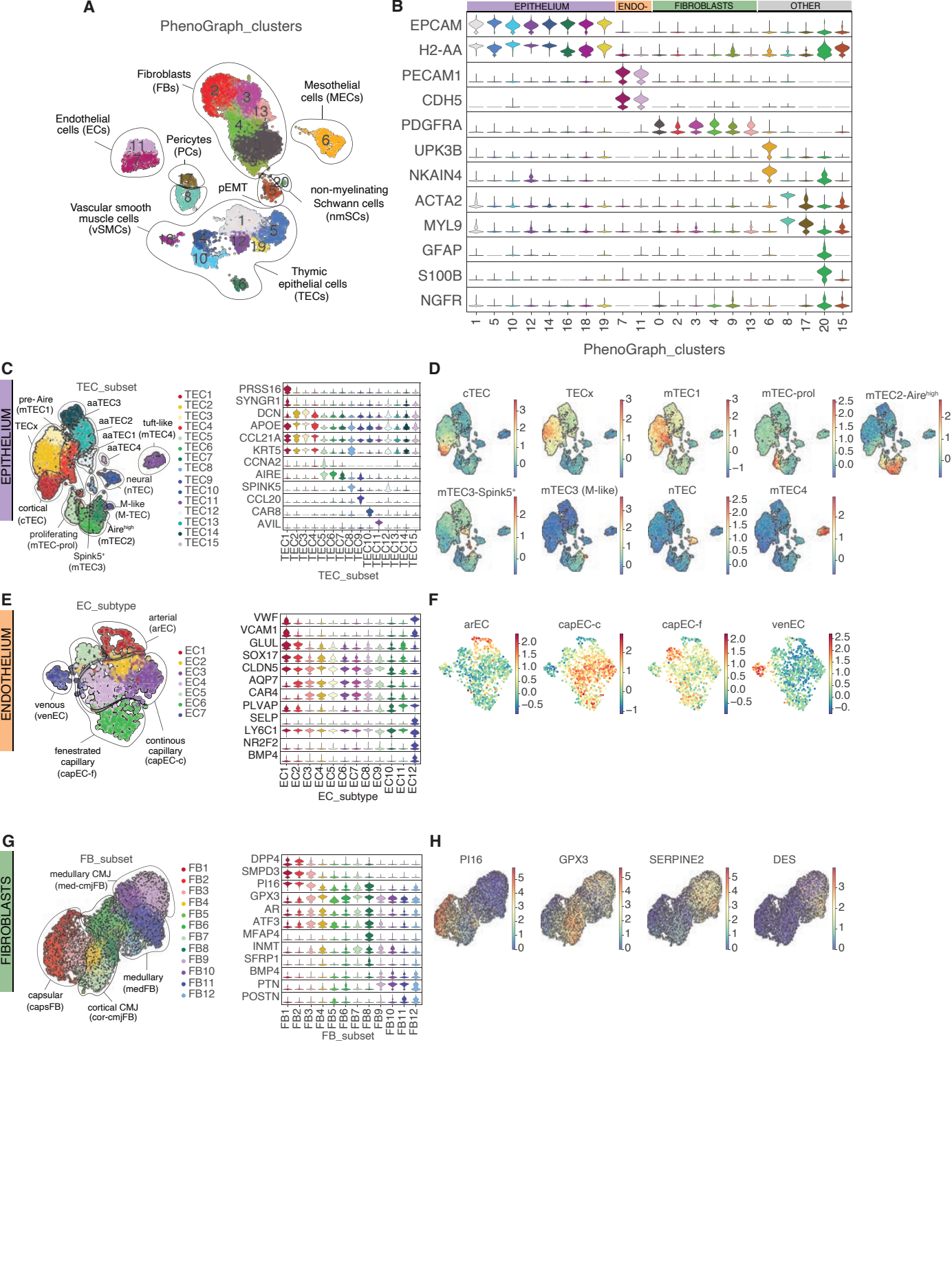
A
PhenoGraph_clusters
Fibroblasts (FBs)
Mesothelial cells (MECs)
Endothelial cells (ECs)
Pericytes (PCs)
pEMT
non-myelinating Schwann cells (nmSCs)
Vascular smooth muscle cells (vSMCs)
Thymic epithelial cells (TECs)
B
EPITHELIUM
ENDO-
FIBROBLASTS
OTHER
EPCAM
H2-AA
PECAM1
CDH5
PDGFRA
UPK3B
NKAIN4
ACTA2
MYL9
GFAP
S100B
NGFR
PhenoGraph_clusters
C
EPITHELIUM
TEC_subset
pre- Aire (mTEC1)
aaTEC3
TECx
aaTEC2
tuft-like
aaTEC1 (mTEC4)
aaTEC4
neural (nTEC)
cortical (cTEC)
M-like (M-TEC)
proliferating (mTEC-prol)
Aire^high (mTEC2)
Spink5+ (mTEC3)
PRSS16
SYNGR1
DCN
APOE
CCL21A
KRT5
CCNA2
AIRE
SPINK5
CCL20
CAR8
AVIL
D
cTEC
TECx
mTEC1
mTEC-prol
mTEC2-Aire^high
mTEC3-Spink5+
mTEC3 (M-like)
nTEC
mTEC4
E
ENDOTHELIUM
EC_subtype
arterial (arEC)
venous (venEC)
fenestrated capillary (capEC-f)
continous capillary (capEC-c)
VWF
VCAM1
GLUL
SOX17
CLDN5
AQP7
CAR4
PLVAP
SELP
LY6C1
NR2F2
BMP4
F
arEC
capEC-c
capEC-f
venEC
G
FIBROBLASTS
FB_subset
medullary CMJ (med-cmjFB)
medullary (medFB)
capsular (capsFB)
cortical CMJ (cor-cmjFB)
DPP4
SMPD3
PI16
GPX3
AR
ATF3
MFAP4
INMT
SFRP1
BMP4
PTN
POSTN
H
PI16
GPX3
SERPINE2
DES

Figure S3. Mapping of the 2-mo steady-state thymic stroma subsets onto the 18-mo steady-state thymic stroma. (**A**) UMAP of 18-mo CD45$^-$ cells labelled by PhenoGraph clusters and main cell types. n_{TOTAL}=11,019 cells. (**B**) Violin plots of canonical markers for main cell types. (**C**, **E** and **G**) UMAPs of 18-mo epithelial (C), endothelial (E) and fibroblast (G) clusters and assorted violin plots of canonical markers and selected DEGs. (**D** and **F**) Gene signatures of top 10 DEGs from the 2-mo epithelium and endothelium defined subsets mapped on the 18-mo thymic epithelium (D) and endothelium (F) respectively. (**H**) Distinctive markers for 2-mo fibroblast defined subsets shown for the 18-mo fibroblasts: Pi16$^+$ (capsFB), Gpx3$^+$ (cor-cmjFB), Des$^+$ (medFB) and Serprine$^+$/Des$^-$ (med-cmjFB).

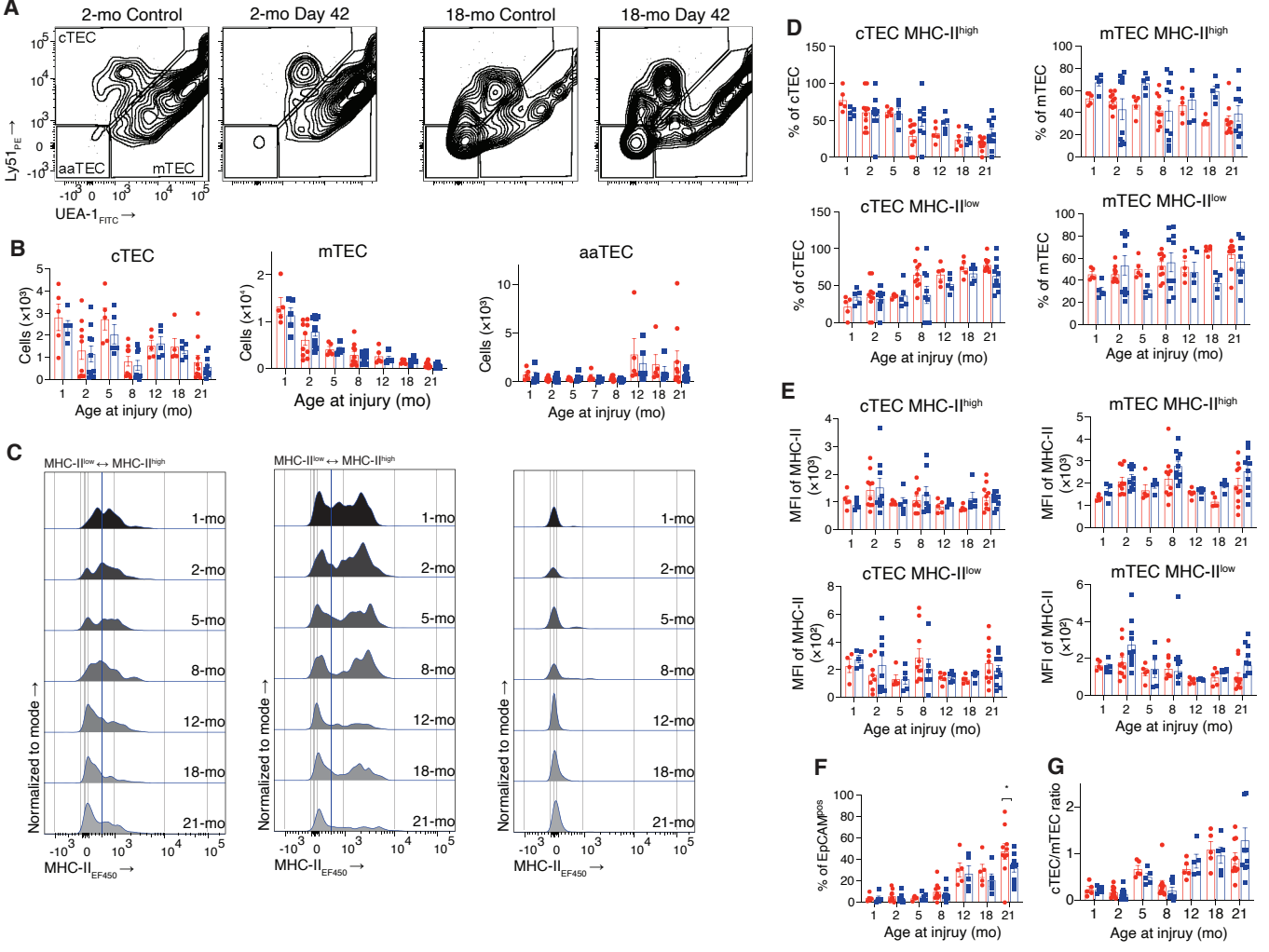
A
2-mo Control
2-mo Day 42
18-mo Control
18-mo Day 42
cTEC
aaTEC
mTEC
Ly51PE →
UEA-1FITC →
B
cTEC
mTEC
aaTEC
Cells (×10³)
Cells (×10⁴)
Age at injury (mo)
C
MHC-IIlow ↔ MHC-IIhigh
1-mo
2-mo
5-mo
8-mo
12-mo
18-mo
21-mo
Normalized to mode →
MHC-IIEF450 →
D
cTEC MHC-IIhigh
mTEC MHC-IIhigh
cTEC MHC-IIlow
mTEC MHC-IIlow
% of cTEC
% of mTEC
Age at injruy (mo)
E
MFI of MHC-II (×10³)
MFI of MHC-II (×10²)
F
% of EpCAMpos
G
cTEC/mTEC ratio

Figure S4. Age-associated compositional changes among thymic epithelium are restored following acute injury. (**A**) Representative dot plots of flow cytometric analysis of enzyme-digested murine thymus of 2-month or 18-month-old female mice at steady-state (Control) or 42 days after SL-TBI (Day 42). Plots show cells gated on single/live/TER119-/CD45-/EpCAM+/MHCII+ cells. Indicated ares Ly51+/UEA1-low cortical TECs (cTECs), Ly51-low/UEA1+ medullary TECs (mTECs), and Ly51-/UEA1- age-associated TECs (aaTECs). (**B**) Cellularity of cTECs, mTECs and aaTECs at steady-state (red) and on day 42 thymic epithelium are restored following acute injury. (**C**) MHC-II expression of cTECs, mTECs and aaTECs on day 42 after SL-TBI, d, frequency of MHC-II-high and MHC-II-low cTECs and mTECs among all cTECs and mTECs respectively at steady-state and day 42 after SL-TBI . (E) Expression of MHC-II on MHC-II-high and MHC-II-low cTECs and mTECs at steady-state and day 42 after SL-TBI. f, frequency of aaTEC among all EpCAM+ thymic epithelial cells. (G) cTEC and mTEC cellularity from (D) and (H) was used to calculate the cTEC/mTEC ratio at steady-state and 42 days after SL-TBI.

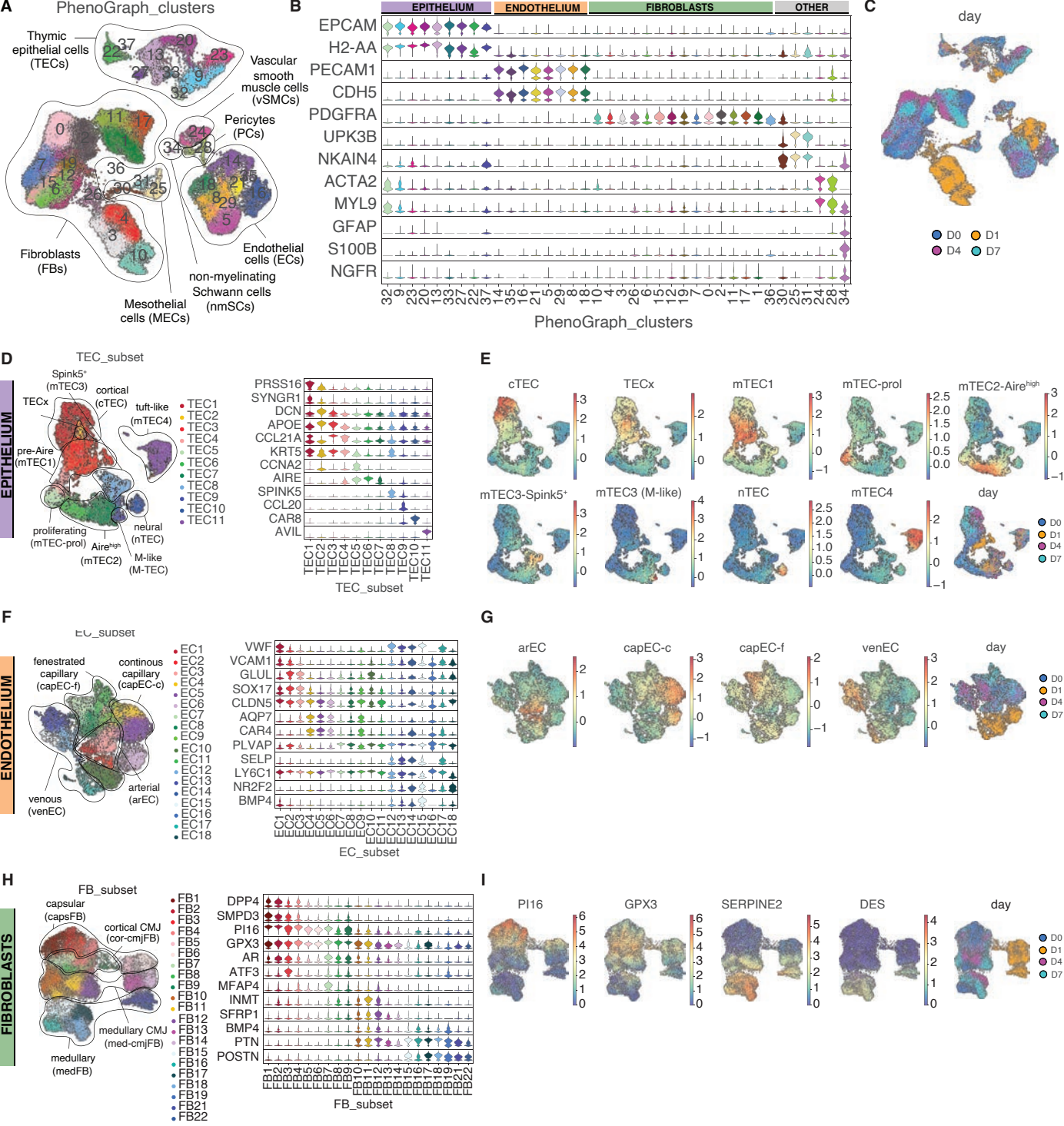
A
PhenoGraph_clusters
Thymic epithelial cells (TECs)
Vascular smooth muscle cells (vSMCs)
Pericytes (PCs)
Fibroblasts (FBs)
Endothelial cells (ECs)
non-myelinating Schwann cells (nmSCs)
Mesothelial cells (MECs)
B
EPITHELIUM
ENDOTHELIUM
FIBROBLASTS
OTHER
EPCAM
H2-AA
PECAM1
CDH5
PDGFRA
UPK3B
NKAIN4
ACTA2
MYL9
GFAP
S100B
NGFR
PhenoGraph_clusters
C
day
D0
D1
D4
D7
D
TEC_subset
EPITHELIUM
Spink5+ (mTEC3)
cortical (cTEC)
TECx
tuft-like (mTEC4)
pre-Aire (mTEC1)
proliferating (mTEC-prol)
Aire^high (mTEC2)
M-like (M-TEC)
neural (nTEC)
PRSS16
SYNGR1
DCN
APOE
CCL21A
KRT5
CCNA2
AIRE
SPINK5
CCL20
CAR8
AVIL
E
cTEC
TECx
mTEC1
mTEC-prol
mTEC2-Aire^high
mTEC3-Spink5+
mTEC3 (M-like)
nTEC
mTEC4
day
F
EC_subset
ENDOTHELIUM
fenestrated capillary (capEC-f)
continous capillary (capEC-c)
venous (venEC)
arterial (arEC)
VWF
VCAM1
GLUL
SOX17
CLDN5
AQP7
CAR4
PLVAP
SELP
LY6C1
NR2F2
BMP4
G
arEC
capEC-c
capEC-f
venEC
day
H
FB_subset
FIBROBLASTS
capsular (capsFB)
cortical CMJ (cor-cmjFB)
medullary CMJ (med-cmjFB)
medullary (medFB)
DPP4
SMPD3
PI16
GPX3
AR
ATF3
MFAP4
INMT
SFRP1
BMP4
PTN
POSTN
I
PI16
GPX3
SERPINE2
DES
day

Figure S5. Mapping of the 2-mo steady-state thymic stroma subsets onto the 2-mo thymic stroma irradiation timeseries. (**A**) UMAP of 2-mo CD45$^-$ thymic cells from the SL-TBI timeseries (steady-state and days 1, 4 and 7 after SL-TBI) labelled by PhenoGraph clusters and main cell types. n_{TOTAL}=38,254 cells. (**B**) Violin plots of canonical markers for main cell types. (**C**) UMAP of 2-mo CD45$^-$ thymic cells from the SL-TBI timeseries labelled by day after SL-TBI. (**D**, **F** and **H**) UMAPs of 2-mo epithelial (D), endothelial (F) and fibroblast (H) clusters from the SL-TBI timeseries and assorted violin plots of canonical markers and selected DEGs. (**E** and **G**) Gene signatures of top 10 DEGs from the 2-mo epithelium and endothelium defined subsets at steady-state mapped on the 2-mo thymic epithelium (D) and endothelium (F) irradiation timeseries respectively. (**H**) Distinctive markers for the 2-mo fibroblast defined subsets at steady-state shown for the 2-mo fibroblast irradiation timeseries: Pi16$^+$ (capsFB), Gpx3$^+$ (cor-cmjFB), Des$^+$ (medFB) and Serprine$^+$/Des$^-$ (med-cmjFB).

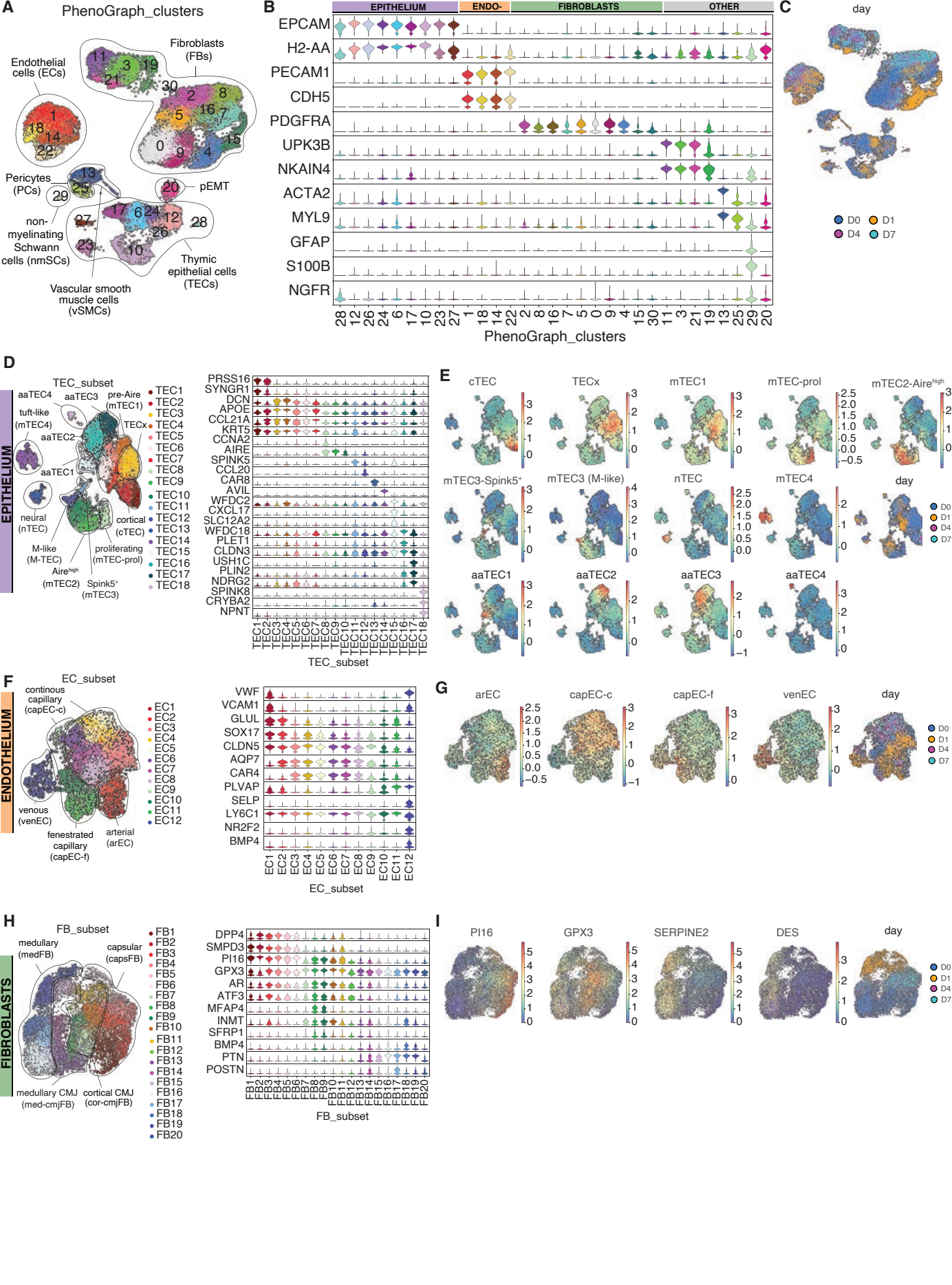
A
PhenoGraph_clusters
Endothelial cells (ECs)
Fibroblasts (FBs)
Pericytes (PCs)
pEMT
non-myelinating Schwann cells (nmSCs)
Thymic epithelial cells (TECs)
Vascular smooth muscle cells (vSMCs)
B
EPITHELIUM
ENDO-
FIBROBLASTS
OTHER
EPCAM
H2-AA
PECAM1
CDH5
PDGFRA
UPK3B
NKAIN4
ACTA2
MYL9
GFAP
S100B
NGFR
PhenoGraph_clusters
C
day
D0
D1
D4
D7
D
TEC_subset
EPITHELIUM
aaTEC4
aaTEC3
pre-Aire (mTEC1)
tuft-like (mTEC4)
aaTEC2
TECx
aaTEC1
neural (nTEC)
cortical (cTEC)
M-like (M-TEC)
proliferating (mTEC-prol)
Aire^high (mTEC2)
Spink5+ (mTEC3)
PRSS16
SYNGR1
DCN
APOE
CCL21A
KRT5
CCNA2
AIRE
SPINK5
CCL20
CAR8
AVIL
WFDC2
CXCL17
SLC12A2
WFDC18
PLET1
CLDN3
USH1C
PLIN2
NDRG2
SPINK8
CRYBA2
NPNT
E
cTEC
TECx
mTEC1
mTEC-prol
mTEC2-Aire^high
mTEC3-Spink5+
mTEC3 (M-like)
nTEC
mTEC4
day
aaTEC1
aaTEC2
aaTEC3
aaTEC4
F
EC_subset
ENDOTHELIUM
continous capillary (capEC-c)
venous (venEC)
fenestrated capillary (capEC-f)
arterial (arEC)
VWF
VCAM1
GLUL
SOX17
CLDN5
AQP7
CAR4
PLVAP
SELP
LY6C1
NR2F2
BMP4
G
arEC
capEC-c
capEC-f
venEC
day
H
FB_subset
FIBROBLASTS
medullary (medFB)
capsular (capsFB)
medullary CMJ (med-cmjFB)
cortical CMJ (cor-cmjFB)
DPP4
SMPD3
PI16
GPX3
AR
ATF3
MFAP4
INMT
SFRP1
BMP4
PTN
POSTN
I
PI16
GPX3
SERPINE2
DES
day

Figure S6. Mapping of the 18-mo steady-state thymic stroma subsets onto the 18-mo thymic stroma irradiation timeseries. (**A**) UMAP of 18-mo CD45$^-$ thymic cells from the SL-TBI timeseries (steady-state and days 1, 4 and 7 after SL-TBI) labelled by PhenoGraph clusters and main cell types. n_{TOTAL}=15,982 cells. (**B**) Violin plots of canonical markers for main cell types. (**C**) UMAP of 18-mo CD45$^-$ thymic cells from the SL-TBI timeseries labelled by day after SL-TBI. (**D**, **F** and **H**) UMAPs of 18-mo epithelial (D), endothelial (F) and fibroblast (H) clusters from the SL-TBI timeseries and assorted violin plots of canonical markers and selected DEGs. (**E** and **G**) Gene signatures of top 10 DEGs from the 18-mo epithelium and endothelium defined subsets at steady-state mapped on the 18-mo thymic epithelium (D) and endothelium (F) irradiation timeseries respectively. (**H**) Distinctive markers for the 18-mo fibroblast defined subsets at steady-state shown for the 18-mo fibroblast irradiation timeseries: Pi16$^+$ (capsFB), Gpx3$^+$ (cor-cmjFB), Des$^+$ (medFB) and Serprine$^+$/Des$^-$ (med-cmjFB).

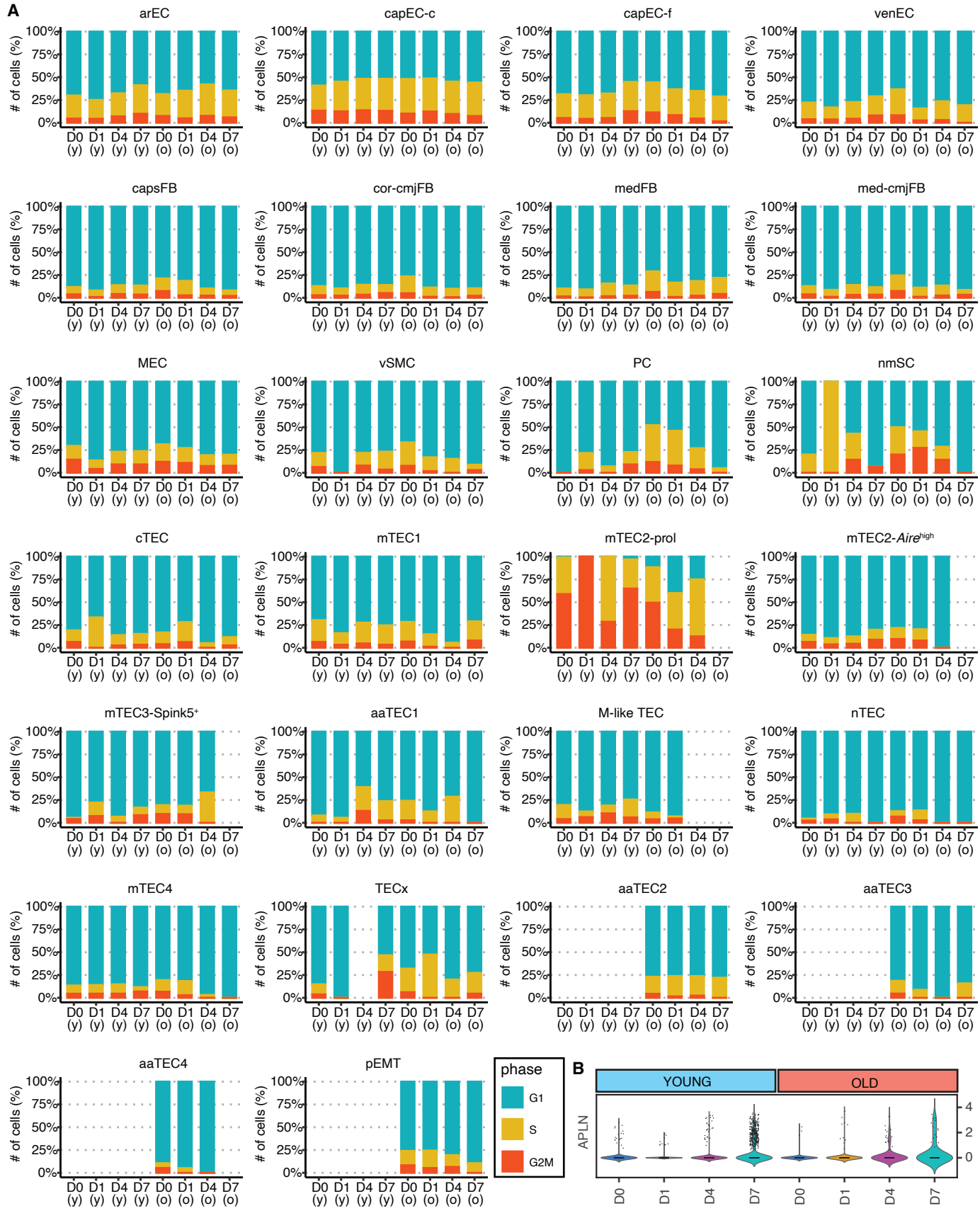
A
arEC
capEC-c
capEC-f
venEC
capsFB
cor-cmjFB
medFB
med-cmjFB
MEC
vSMC
PC
nmSC
cTEC
mTEC1
mTEC2-prol
mTEC2-Aire^high
mTEC3-Spink5+
aaTEC1
M-like TEC
nTEC
mTEC4
TECx
aaTEC2
aaTEC3
aaTEC4
pEMT
# of cells (%)
100%
75%
50%
25%
0%
D0 (y)
D1 (y)
D4 (y)
D7 (y)
D0 (o)
D1 (o)
D4 (o)
D7 (o)
phase
G1
S
G2M
B
YOUNG
OLD
APLN
4
2
0
D0
D1
D4
D7
D0
D1
D4
D7

Figure S7. Distribution of cells across cell cycle phases. (**A**) Stacked barplots showing the percentage of cells assigned to each cell cycle phase (G1; ciel, S; yellow and G2/M; orange) for all $CD45^-$ subsets at steady state (D0) and at days 1 (D1), 4 (D4) and 7 (D7) after SL-TBI both in 2-mo (young; y) and 18-mo (old; o) mice. Percentage of cells assigned to each phase is shown on the *y*-axis. Subset-specific stage (young/old) and SL-TBI timepoint is shown on the *x*-axis. Cell assignment to each phase is described in Methods. (**B**) Violin plots of Apln expression in capECs-f at steady state (D0) and at days 1 (D1), 4 (D4) and 7 (D7) after SL-TBI both in 2-mo (young) and 18-mo (old) mice.

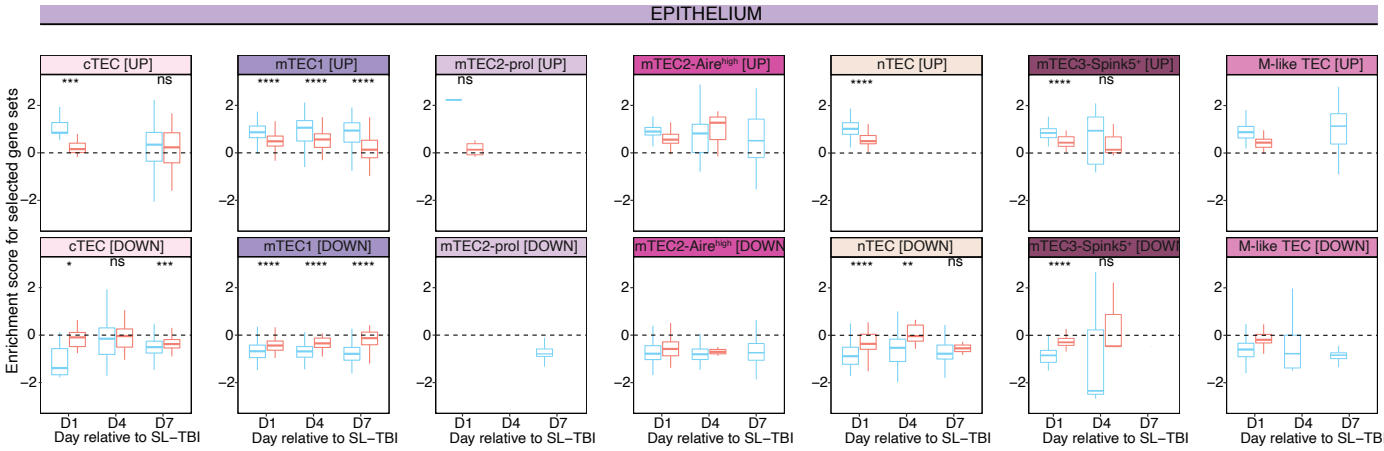
EPITHELIUM
cTEC [UP]
mTEC1 [UP]
mTEC2-prol [UP]
mTEC2-Aire^high [UP]
nTEC [UP]
mTEC3-Spink5+ [UP]
M-like TEC [UP]
cTEC [DOWN]
mTEC1 [DOWN]
mTEC2-prol [DOWN]
mTEC2-Aire^high [DOWN
nTEC [DOWN]
mTEC3-Spink5+ [DOW
M-like TEC [DOWN]
Enrichment score for selected gene sets
Day relative to SL−TBI
D1
D4
D7

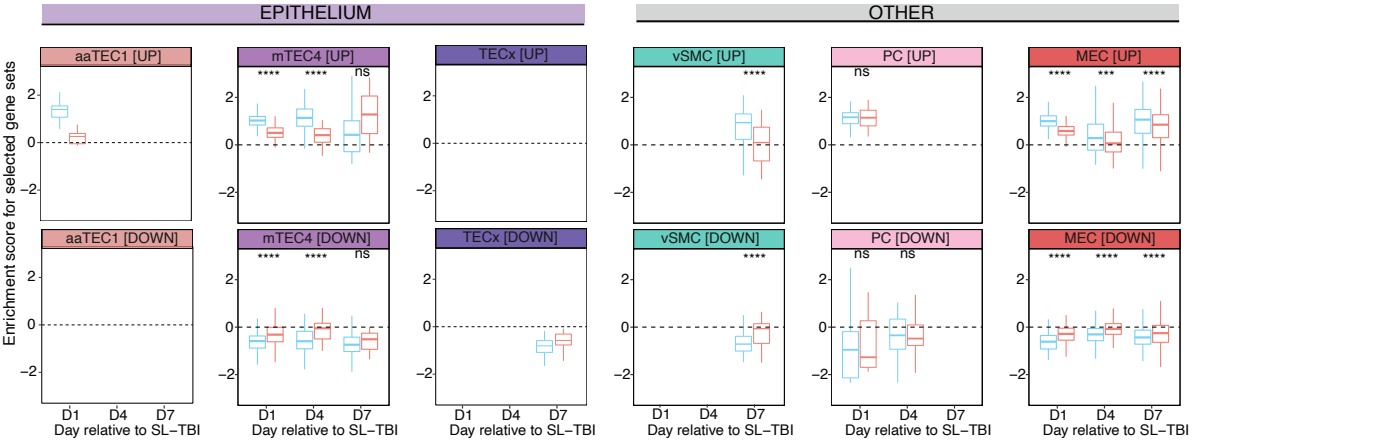
EPITHELIUM
OTHER
aaTEC1 [UP]
mTEC4 [UP]
TECx [UP]
vSMC [UP]
PC [UP]
MEC [UP]
aaTEC1 [DOWN]
mTEC4 [DOWN]
TECx [DOWN]
vSMC [DOWN]
PC [DOWN]
MEC [DOWN]
Enrichment score for selected gene sets
Day relative to SL−TBI
D1
D4
D7

Figure S8. Boxplots showing the MAST enrichment scores for up- and down-regulated genes based on the 2-mo day 1 (D1), day 4 (D4) and day 7 (D7) comparisons versus the respective steady-state (D0) for all epithelial and other subsets.

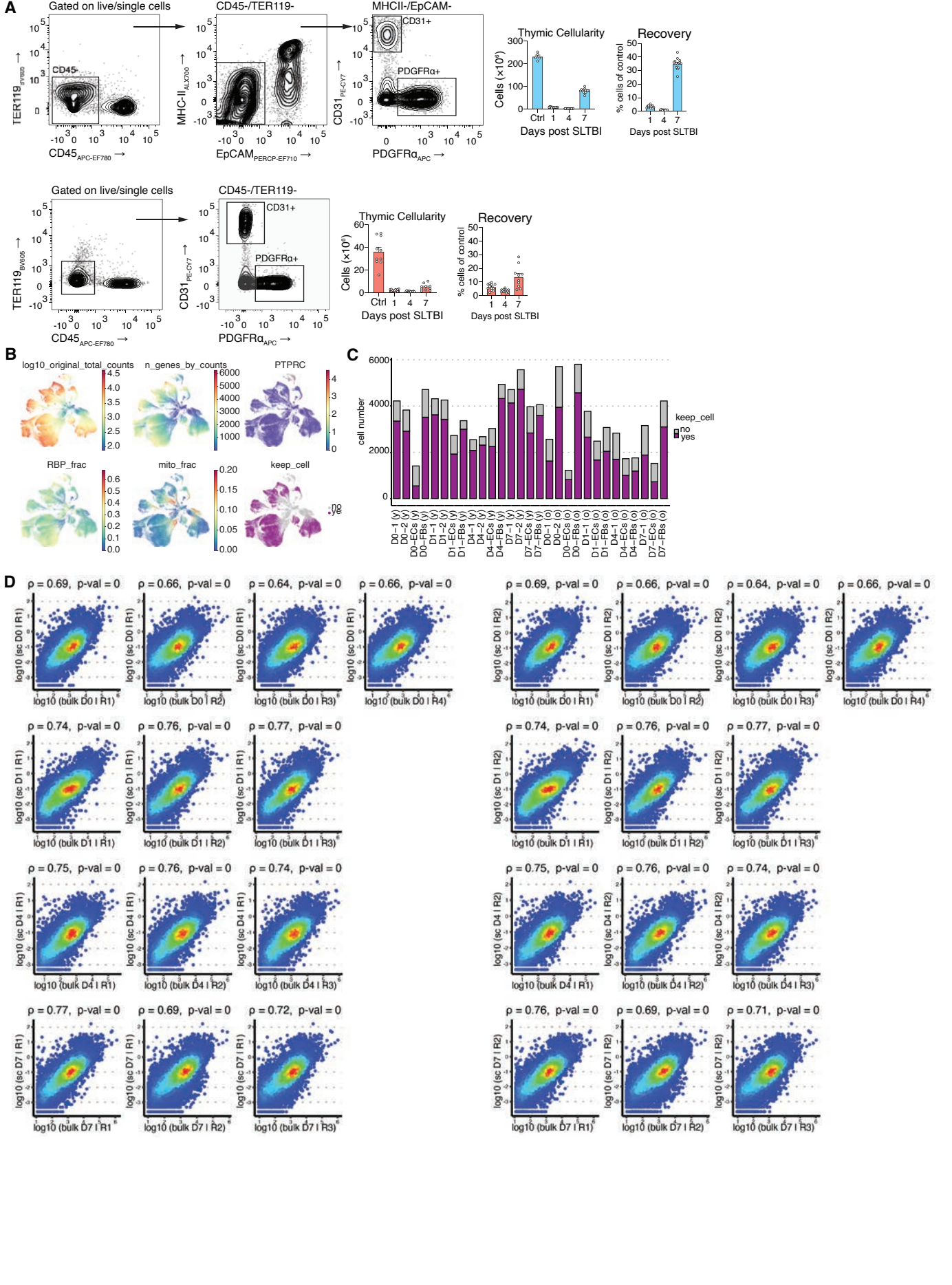
A
Gated on live/single cells
CD45-/TER119-
MHCII-/EpCAM-
CD45-
CD31+
PDGFRα+
Thymic Cellularity
Recovery
Cells (x10⁶)
% cells of control
Ctrl 1 4 7
Days post SLTBI
B
log10_original_total_counts
n_genes_by_counts
PTPRC
RBP_frac
mito_frac
keep_cell
C
cell number
keep_cell
no
yes
D
ρ = 0.69, p-val = 0
ρ = 0.66, p-val = 0
ρ = 0.64, p-val = 0
ρ = 0.74, p-val = 0
ρ = 0.76, p-val = 0
ρ = 0.77, p-val = 0
ρ = 0.75, p-val = 0
ρ = 0.69, p-val = 0
ρ = 0.72, p-val = 0
ρ = 0.71, p-val = 0
log10 (sc D0 I R1)
log10 (sc D0 I R2)
log10 (sc D1 I R1)
log10 (sc D1 I R2)
log10 (sc D4 I R1)
log10 (sc D4 I R2)
log10 (sc D7 I R1)
log10 (sc D7 I R2)
log10 (bulk D0 I R1)
log10 (bulk D0 I R2)
log10 (bulk D0 I R3)
log10 (bulk D0 I R4)
log10 (bulk D1 I R1)
log10 (bulk D1 I R2)
log10 (bulk D1 I R3)
log10 (bulk D4 I R1)
log10 (bulk D4 I R2)
log10 (bulk D4 I R3)
log10 (bulk D7 I R1)
log10 (bulk D7 I R2)
log10 (bulk D7 I R3)

Figure S9. Quality control of scRNA-seq samples and correlation with bulk RNA-seq data. (**A**) FACs sorting protocol for $CD45^-$ thymic stroma, thymic endothelium and fibroblasts in 2-mo and 18-mo mice. (**B**) UMAPs of all scRNA-seq samples (combined) prior to removal of bad quality cells, doublets and $CD45^+$ contaminants, color-coded for total counts, number of genes, ribosomal fraction, mitochondrial fraction per cell, as well as $CD45^+$ contaminating cells expressing the *Ptprc* gene and good quality cells retained for further analysis. (**C**) Stacked barplot representation of filtered out cells on a per sample basis. Cells retained for further processing are shown in purple, while cells removed are shown in grey. (**D**) Scatterplots showing correlation (Pearson) between averaged expression profiles of $CD45^-$ scRNA-seq technical replicates 1 (left) and 2 (right) collected at steady state (row 1), day 1 (row 2), day 4 (row 3) and day 7 (row 4) after SLTBI versus the expression profiles of $CD45^-$ bulk RNA-seq biological replicates (replicate 1; column 1, replicate 2; column 2, replicate 3; column 3, replicate 4; column 4) obtained on the same timeframe.

Data S1. Canonical markers for thymic stroma subsets. Includes lists of canonical marker genes from thymic epithelial, endothelial and fibroblast defined subsets and how our thymic stroma subsets map to previous published work.

Data S2. Table of DEGs for the 2-mo thymic epithelial subsets at steady-state. Includes MAST results from all pairwise comparisons of the 2-mo thymic epithelial subsets at steady-state. The top 10 DEGs per subset (sorted by coef in decreasing order) were used to create subset-specific gene signatures as described in the Methods and the main text.

Data S3. Table of DEGs for the 2-mo thymic endothelial subsets at steady-state. Includes MAST results from all pairwise comparisons of the 2-mo thymic endothelial subsets at steady-state. The top 10 DEGs per subset (sorted by coef in decreasing order) were used to create subset-specific gene signatures as described in the Methods and the main text.

Data S4. Table of DEGs for the 2-mo thymic fibroblast subsets at steady-state. Includes MAST results from all pairwise comparisons of the 2-mo thymic fibroblast subsets at steady-state. The top 10 DEGs per subset (sorted by coef in decreasing order) were used to create subset-specific gene signatures as described in the Methods and the main text.

Data S5. Table of DEGs for the 18-mo thymic epithelial subsets at steady-state. Includes MAST results from all pairwise comparisons of the 18-mo thymic epithelial subsets at steady-state. The top 10 DEGs per subset (sorted by coef in decreasing order) were used to create subset-specific gene signatures as described in the Methods and the main text.

Data S6. Table of DEGs for the 18-mo thymic endothelial subsets at steady-state. Includes MAST results from all pairwise comparisons of the 18-mo thymic endothelial subsets at steady-

state. The top 10 DEGs per subset (sorted by coef in decreasing order) were used to create subset-specific gene signatures as described in the Methods and the main text.

Data S7. GSEA enriched pathways with aging. Includes EnrichmentMap-generated network table with the combined GSEA results from all 18-mo vs 2-mo steady-state subset comparisons. To assist result interpretation, pathways have been manually categorized and labeled based on gene overlap and pathway relevance in respect to Aging Hallmarks.

Data S8. GSEA enriched pathways after damage within each age cohort. Includes EnrichmentMap-generated network table with the combined GSEA results from all transition comparisons per age cohort. To assist result interpretation, pathways have been manually categorized and labeled based on gene overlap and pathway function into more broad categories.

REFERENCES

Abramson, J., and Anderson, G. (2017). Thymic Epithelial Cells. Annu. Rev. Immunol. *35*, 85–118.

Andrews, S. (2010). FastQC: a quality control tool for high throughput sequence data.

Azizi, E., Carr, A.J., Plitas, G., Cornish, A.E., Konopacki, C., Prabhakaran, S., Nainys, J., Wu, K., Kiseliovas, V., Setty, M., et al. (2018). Single-Cell Map of Diverse Immune Phenotypes in the Breast Tumor Microenvironment. Cell *174*, 1293-1308.e36.

Baran-Gale, J., Morgan, M.D., Maio, S., Dhalla, F., Calvo-Asensio, I., Deadman, M.E., Handel, A.E., Maynard, A., Chen, S., Green, F., et al. (2020). Ageing compromises mouse thymus function and remodels epithelial cell differentiation. ELife *9*.

Berent-Maoz, B., Montecino-Rodriguez, E., and Dorshkind, K. (2012). Genetic regulation of thymocyte progenitor aging. Semin. Immunol. *24*, 303–308.

Boehm, T., and Swann, J.B. (2013). Thymus involution and regeneration: two sides of the same coin? Nat. Rev. Immunol. *13*, 831–838.

Bolger, A.M., Lohse, M., and Usadel, B. (2014). Trimmomatic: a flexible trimmer for Illumina sequence data. Bioinformatics *30*, 2114–2120.

Bornstein, C., Nevo, S., Giladi, A., Kadouri, N., Pouzolles, M., Gerbe, F., David, E., Machado, A., Chuprin, A., Tóth, B., et al. (2018). Single-cell mapping of the thymic stroma identifies IL-25-producing tuft epithelial cells. Nature *559*, 622–626.

Bosma, E.K., van Noorden, C.J.F., Schlingemann, R.O., and Klaassen, I. (2018). The role of plasmalemma vesicle-associated protein in pathological breakdown of blood–brain and blood–retinal barriers: potential novel therapeutic target for cerebral edema and diabetic macular

edema. Fluids Barriers CNS *15*, 24.

Bowyer, J.F., Patterson, T.A., Saini, U.T., Hanig, J.P., Thomas, M., Camacho, L., George, N.I., and Chen, J.J. (2013). Comparison of the global gene expression of choroid plexus and meninges and associated vasculature under control conditions and after pronounced hyperthermia or amphetamine toxicity. BMC Genomics *14*, 147.

Brennecke, P., Reyes, A., Pinto, S., Rattay, K., Nguyen, M., Küchler, R., Huber, W., Kyewski, B., and Steinmetz, L.M. (2015). Single-cell transcriptome analysis reveals coordinated ectopic gene-expression patterns in medullary thymic epithelial cells. Nat. Immunol. *16*, 933–941.

Buono, M., Facchini, R., Matsuoka, S., Thongjuea, S., Waithe, D., Luis, T.C., Giustacchini, A., Besmer, P., Mead, A.J., Jacobsen, S.E.W., et al. (2016). A dynamic niche provides Kit ligand in a stage-specific manner to the earliest thymocyte progenitors. Nat. Cell Biol. *18*, 157–167.

Buono, M., Thézénas, M.-L., Ceroni, A., Fischer, R., and Nerlov, C. (2018). Bi-directional signaling by membrane-bound KitL induces proliferation and coordinates thymic endothelial cell and thymocyte expansion. Nat. Commun. *9*, 4685.

Cané, S., Ponnappan, S., and Ponnappan, U. (2012). Altered regulation of CXCR4 expression during aging contributes to increased CXCL12-dependent chemotactic migration of CD4(+) T cells. Aging Cell *11*, 651–658.

Chen, B.J., Cui, X., Sempowski, G.D., Domen, J., and Chao, N.J. (2004). Hematopoietic stem cell dose correlates with the speed of immune reconstitution after stem cell transplantation. Blood *103*, 4344–4352.

Chen, Q., Liu, Y., Jeong, H.-W., Stehling, M., Dinh, V.V., Zhou, B., and Adams, R.H. (2019). Apelin+ Endothelial Niche Cells Control Hematopoiesis and Mediate Vascular Regeneration after Myeloablative Injury. Cell Stem Cell *25*, 768-783.e6.

Depreter, M.G.L., Blair, N.F., Gaskell, T.L., Nowell, C.S., Davern, K., Pagliocca, A., Stenhouse, F.H., Farley, A.M., Fraser, A., Vrana, J., et al. (2008). Identification of Plet-1 as a specific marker of early thymic epithelial progenitor cells. Proc. Natl. Acad. Sci. *105*, 961–966.

Dhalla, F., Baran-Gale, J., Maio, S., Chappell, L., Holländer, G.A., and Ponting, C.P. (2020). Biologically indeterminate yet ordered promiscuous gene expression in single medullary thymic epithelial cells. EMBO J. *39*.

Dobin, A., Davis, C.A., Schlesinger, F., Drenkow, J., Zaleski, C., Jha, S., Batut, P., Chaisson, M., and Gingeras, T.R. (2013). STAR: ultrafast universal RNA-seq aligner. Bioinforma. Oxf. Engl. *29*, 15–21.

Douek, D.C., McFarland, R.D., Keiser, P.H., Gage, E.A., Massey, J.M., Haynes, B.F., Polis, M.A., Haase, A.T., Feinberg, M.B., Sullivan, J.L., et al. (1998). Changes in thymic function with age and during the treatment of HIV infection. Nature *396*, 690–695.

Ferrando-Martínez, S., Ruiz-Mateos, E., Dudakov, J.A., Velardi, E., Grillari, J., Kreil, D.P., Muñoz-Fernandez, M.Á., van den Brink, M.R.M., and Leal, M. (2015). WNT signaling suppression in the senescent human thymus. J. Gerontol. A. Biol. Sci. Med. Sci. *70*, 273–281.

Finak, G., McDavid, A., Yajima, M., Deng, J., Gersuk, V., Shalek, A.K., Slichter, C.K., Miller, H.W., McElrath, M.J., Prlic, M., et al. (2015). MAST: a flexible statistical framework for assessing transcriptional changes and characterizing heterogeneity in single-cell RNA sequencing data. Genome Biol. *16*, 278.

Gayoso, A., and Shor, J. (2020). JonathanShor/DoubletDetection: doubletdetection v3.0 (Zenodo).

Gordon, L., Blechman, J., Shimoni, E., Gur, D., Anand-Apte, B., and Levkowitz, G. (2019). The fenestrae-associated protein Plvap regulates the rate of blood-borne protein passage into the

hypophysis. Development *146*, dev177790.

Granadier, D., Iovino, L., Kinsella, S., and Dudakov, J.A. (2021). Dynamics of thymus function and T cell receptor repertoire breadth in health and disease. Semin. Immunopathol. *43*, 119–134.

Gray, D.H.D., Fletcher, A.L., Hammett, M., Seach, N., Ueno, T., Young, L.F., Barbuto, J., Boyd, R.L., and Chidgey, A.P. (2008). Unbiased analysis, enrichment and purification of thymic stromal cells. J. Immunol. Methods *329*, 56–66.

Gruver, A., Hudson, L., and Sempowski, G. (2007). Immunosenescence of ageing. J. Pathol. *211*, 144–156.

Haber, A.L., Biton, M., Rogel, N., Herbst, R.H., Shekhar, K., Smillie, C., Burgin, G., Delorey, T.M., Howitt, M.R., Katz, Y., et al. (2017). A single-cell survey of the small intestinal epithelium. Nature *551*, 333–339.

Hale, J.S., Boursalian, T.E., Turk, G.L., and Fink, P.J. (2006). Thymic output in aged mice. Proc. Natl. Acad. Sci. U. S. A. *103*, 8447–8452.

Hamazaki, Y., Fujita, H., Kobayashi, T., Choi, Y., Scott, H.S., Matsumoto, M., and Minato, N. (2007). Medullary thymic epithelial cells expressing Aire represent a unique lineage derived from cells expressing claudin. Nat. Immunol. *8*, 304–311.

Hipp, M.S., Kasturi, P., and Hartl, F.U. (2019). The proteostasis network and its decline in ageing. Nat. Rev. Mol. Cell Biol. *20*, 421–435.

Hu, D., Nicholls, P.K., Yin, C., Kelman, K., Yuan, Q., Greene, W.K., Shi, Z., and Ma, B. (2018). Immunofluorescent Localization of Non-myelinating Schwann Cells and Their Interactions With Immune Cells in Mouse Thymus. J. Histochem. Cytochem. *66*, 775–785.

Jain, R., and Gray, D.H.D. (2014). Isolation of thymic epithelial cells and analysis by flow cytometry. Curr. Protoc. Immunol. *107*, 3.26.1-3.26.15.

Kadouri, N., Nevo, S., Goldfarb, Y., and Abramson, J. (2020). Thymic epithelial cell heterogeneity: TEC by TEC. Nat. Rev. Immunol. *20*, 239–253.

Kalucka, J., de Rooij, L.P.M.H., Goveia, J., Rohlenova, K., Dumas, S.J., Meta, E., Conchinha, N.V., Taverna, F., Teuwen, L.-A., Veys, K., et al. (2020). Single-Cell Transcriptome Atlas of Murine Endothelial Cells. Cell *180*, 764-779.e20.

Kinsella, S., and Dudakov, J.A. (2020). When the Damage Is Done: Injury and Repair in Thymus Function. Front. Immunol. *11*, 1745.

Koliaraki, V., Prados, A., Armaka, M., and Kollias, G. (2020). The mesenchymal context in inflammation, immunity and cancer. Nat. Immunol. *21*, 974–982.

Krausgruber, T., Fortelny, N., Fife-Gernedl, V., Senekowitsch, M., Schuster, L.C., Lercher, A., Nemc, A., Schmidl, C., Rendeiro, A.F., Bergthaler, A., et al. (2020). Structural cells are key regulators of organ-specific immune responses. Nature *583*, 296–302.

Levine, J.H., Simonds, E.F., Bendall, S.C., Davis, K.L., Amir, E.D., Tadmor, M.D., Litvin, O., Fienberg, H.G., Jager, A., Zunder, E.R., et al. (2015). Data-Driven Phenotypic Dissection of AML Reveals Progenitor-like Cells that Correlate with Prognosis. Cell *162*, 184–197.

Liao, Y., Smyth, G.K., and Shi, W. (2014). featureCounts: an efficient general purpose program for assigning sequence reads to genomic features. Bioinformatics *30*, 923–930.

Liu, Z., Farley, A., Chen, L., Kirby, B.J., Kovacs, C.S., Blackburn, C.C., and Manley, N.R. (2010). Thymus-Associated Parathyroid Hormone Has Two Cellular Origins with Distinct Endocrine and Immunological Functions. PLoS Genet. *6*, e1001251.

López-Otín, C., Blasco, M.A., Partridge, L., Serrano, M., and Kroemer, G. (2013). The Hallmarks of Aging. Cell *153*, 1194–1217.

Merico, D., Isserlin, R., Stueker, O., Emili, A., and Bader, G.D. (2010). Enrichment map: a

network-based method for gene-set enrichment visualization and interpretation. PloS One *5*, e13984.

Miragaia, R.J., Zhang, X., Gomes, T., Svensson, V., Ilicic, T., Henriksson, J., Kar, G., and Lönnberg, T. (2018). Single-cell RNA-sequencing resolves self-antigen expression during mTEC development. Sci. Rep. *8*, 685.

Nikolich-Zugich, J. (2008). Ageing and life-long maintenance of T-cell subsets in the face of latent persistent infections. Nat. Rev. Immunol. *8*, 512–522.

Nitta, T., and Takayanagi, H. (2021). Non-Epithelial Thymic Stromal Cells: Unsung Heroes in Thymus Organogenesis and T Cell Development. Front. Immunol. *11*, 620894.

Nitta, T., Tsutsumi, M., Nitta, S., Muro, R., Suzuki, E.C., Nakano, K., Tomofuji, Y., Sawa, S., Okamura, T., Penninger, J.M., et al. (2020). Fibroblasts as a source of self-antigens for central immune tolerance. Nat. Immunol.

Park, J.-E., Botting, R.A., Domínguez Conde, C., Popescu, D.-M., Lavaert, M., Kunz, D.J., Goh, I., Stephenson, E., Ragazzini, R., Tuck, E., et al. (2020). A cell atlas of human thymic development defines T cell repertoire formation. Science *367*, eaay3224.

Penit, C., and Ezine, S. (1989). Cell proliferation and thymocyte subset reconstitution in sublethally irradiated mice: compared kinetics of endogenous and intrathymically transferred progenitors. Proc. Natl. Acad. Sci. U. S. A. *86*, 5547–5551.

Raudvere, U., Kolberg, L., Kuzmin, I., Arak, T., Adler, P., Peterson, H., and Vilo, J. (2019). g:Profiler: a web server for functional enrichment analysis and conversions of gene lists (2019 update). Nucleic Acids Res. *47*, W191–W198.

Reimand, J., Kull, M., Peterson, H., Hansen, J., and Vilo, J. (2007). g:Profiler—a web-based toolset for functional profiling of gene lists from large-scale experiments. Nucleic Acids Res. *35*,

W193–W200.

Robinson, M.D., McCarthy, D.J., and Smyth, G.K. (2010). edgeR: a Bioconductor package for differential expression analysis of digital gene expression data. Bioinforma. Oxf. Engl. *26*, 139–140.

Rodewald, H.R. (1998). The thymus in the age of retirement. Nature *396*, 630–631.

Sansom, S.N., Shikama-Dorn, N., Zhanybekova, S., Nusspaumer, G., Macaulay, I.C., Deadman, M.E., Heger, A., Ponting, C.P., and Holländer, G.A. (2014). Population and single-cell genomics reveal the Aire dependency, relief from Polycomb silencing, and distribution of self-antigen expression in thymic epithelia. Genome Res. *24*, 1918–1931.

Setty, M., Kiseliovas, V., Levine, J., Gayoso, A., Mazutis, L., and Pe'er, D. (2019). Characterization of cell fate probabilities in single-cell data with Palantir. Nat. Biotechnol. *37*, 451–460.

Shannon, P., Markiel, A., Ozier, O., Baliga, N.S., Wang, J.T., Ramage, D., Amin, N., Schwikowski, B., and Ideker, T. (2003). Cytoscape: a software environment for integrated models of biomolecular interaction networks. Genome Res. *13*, 2498–2504.

Sheng, L., and Zhuang, S. (2020). New Insights Into the Role and Mechanism of Partial Epithelial-Mesenchymal Transition in Kidney Fibrosis. Front. Physiol. *11*, 569322.

Shi, Y., Wu, W., Chai, Q., Li, Q., Hou, Y., Xia, H., Ren, B., Xu, H., Guo, X., Jin, C., et al. (2016). LTβR controls thymic portal endothelial cells for haematopoietic progenitor cell homing and T-cell regeneration. Nat. Commun. *7*, 12369.

Subramanian, A., Tamayo, P., Mootha, V.K., Mukherjee, S., Ebert, B.L., Gillette, M.A., Paulovich, A., Pomeroy, S.L., Golub, T.R., Lander, E.S., et al. (2005). Gene set enrichment analysis: a knowledge-based approach for interpreting genome-wide expression profiles. Proc.

Natl. Acad. Sci. U. S. A. *102*, 15545–15550.

The Tabula Muris Consortium (2020). A single-cell transcriptomic atlas characterizes ageing tissues in the mouse. Nature *583*, 590–595.

Tirosh, I., Izar, B., Prakadan, S.M., Wadsworth, M.H., Treacy, D., Trombetta, J.J., Rotem, A., Rodman, C., Lian, C., Murphy, G., et al. (2016). Dissecting the multicellular ecosystem of metastatic melanoma by single-cell RNA-seq. Science *352*, 189–196.

Valletta, S., Thomas, A., Meng, Y., Ren, X., Drissen, R., Sengül, H., Di Genua, C., and Nerlov, C. (2020). Micro-environmental sensing by bone marrow stroma identifies IL-6 and TGFβ1 as regulators of hematopoietic ageing. Nat. Commun. *11*, 4075.

Vanlandewijck, M., He, L., Mäe, M.A., Andrae, J., Ando, K., Del Gaudio, F., Nahar, K., Lebouvier, T., Laviña, B., Gouveia, L., et al. (2018). A molecular atlas of cell types and zonation in the brain vasculature. Nature *554*, 475–480.

Velardi, E., Tsai, J.J., and van den Brink, M.R.M. (2021). T cell regeneration after immunological injury. Nat. Rev. Immunol. *21*, 277–291.

Ventevogel, M.S., and Sempowski, G.D. (2013). Thymic rejuvenation and aging. Curr. Opin. Immunol. *25*, 516–522.

Wertheimer, T., Velardi, E., Tsai, J., Cooper, K., Xiao, S., Kloss, C.C., Ottmüller, K.J., Mokhtari, Z., Brede, C., deRoos, P., et al. (2018). Production of BMP4 by endothelial cells is crucial for endogenous thymic regeneration. Sci. Immunol. *3*.

Wolf, F.A., Angerer, P., and Theis, F.J. (2018). SCANPY: large-scale single-cell gene expression data analysis. Genome Biol. *19*, 15.

Youm, Y.-H., Yang, H., Sun, Y., Smith, R.G., Manley, N.R., Vandanmagsar, B., and Dixit, V.D. (2009). Deficient Ghrelin Receptor-mediated Signaling Compromises Thymic Stromal Cell

Microenvironment by Accelerating Thymic Adiposity. J. Biol. Chem. *284*, 7068–7077.

Zachariah, M.A., and Cyster, J.G. (2010). Neural crest-derived pericytes promote egress of mature thymocytes at the corticomedullary junction. Science *328*, 1129–1135.

Zlotoff, D.A., Zhang, S.L., De Obaldia, M.E., Hess, P.R., Todd, S.P., Logan, T.D., and Bhandoola, A. (2011). Delivery of progenitors to the thymus limits T-lineage reconstitution after bone marrow transplantation. Blood *118*, 1962–1970.